Evaluation of phenospectral dynamics with Sentinel-2A using a bottom-up approach in a northern ombrotrophic peatland

Arroyo-Mora, J. P.; Kalacska, M.; Soffer, R.; Ifimov, G.; Leblanc, G.; Schaaf, E. S.; Lucanus, O.

Publisher's version / Version de l'éditeur:
https://doi.org/10.1016/j.rse.2018.07.021
Remote Sensing of Environment, 216, pp. 544-560, 2018-07-24

Remote Sensing of Environment 216 (2018) 544–560

Contents lists available at ScienceDirect

Remote Sensing of Environment

journal homepage: www.elsevier.com/locate/rse

Evaluation of phenospectral dynamics with Sentinel-2A using a bottom-up approach in a northern ombrotrophic peatland

J.P. Arroyo-Mora[a,*], M. Kalacska[b], R. Soffer[a], G. Ifimov[a], G. Leblanc[a], E.S. Schaaf[b], O. Lucanus[b]

[a] National Research Council of Canada, Flight Research Laboratory, 1920 Research Rd, Ottawa, ON, Canada
[b] Applied Remote Sensing Laboratory (ARSL), Department of Geography, McGill University, Montreal, QC, Canada

ARTICLE INFO

Keywords:
Sentinel-2 MSI
Mer Bleue
Phenospectral
Spectroscopy
Airborne hyperspectral
CASI
Multi-datasets
Bog
Land product validation

ABSTRACT

Peatlands cover very large extents in northern regions and play a significant role in the global carbon cycle by functioning as a carbon sink. Large-scale satellite based monitoring systems, such as the Sentinel-2 Multispectral Instrument (MSI), are necessary to improve our understanding of how these ecosystems respond to climate change by providing verifiable land products. For instance, satellite-based land product validation approaches can benefit from airborne hyperspectral imagery and in-situ data, which provide higher spatial and spectral resolution baselines, ideal for measuring vegetation changes (e.g. phenology, LAI) at local scales. Here, we assessed the short-term phenospectral dynamics (spectral changes indicated by specific spectral features as a function of phenology) of five ombrotrophic peatland vegetation physiognomies over four dates at the Mer Bleue bog in Canada. We took advantage of a unique remote sensing data acquisition campaign aiming to validate Sentinel-2A land products, and analyzed three spatially and spectrally distinctive datasets (i.e. field spectra, VISNIR airborne hyperspectral imagery (HSI) and Sentinel-2A imagery) over the first half of the 2016 growing season. By implementing a bottom-up approach, first we assessed the airborne HSI's capability to detect phenological changes as compared to in-situ acquired field spectroscopy measurements in a 10 ha area at Mer Bleue and evaluated the spectral features characteristic of these phenological changes. Second, over the entire Mer Bleue area (28,000 ha), we compared a series of four Sentinel-2A images to four airborne HSI mosaics (spatially and spectrally resampled to Sentinel-2A) to assess the utility of Sentinel-2A for detecting small spectral variations due to phenological changes (i.e. greening). In addition, for this second comparison, three spectral vegetation indices were derived from the Sentinel-2A images and the airborne HSI mosaics. The spectral comparisons between the airborne HSI and the field spectroscopy data revealed clear phenological changes from the airborne HSI. For instance, a closer agreement between reflectance measured by the field spectrometer and the airborne HSI spectral response was found in the visible region (450–680 nm). A greater difference however, was consistently seen in the near-infrared region (681–866 nm) across the four dates. Narrow spectral features in three regions of the visible range (global minima, red absorption, green peak), indicating changes in vegetation colour, were consistent for both datasets and with expected phenological patterns at Mer Bleue. At the landscape level, Sentinel-2A mirrored the spectral changes depicted by the resampled HSI data. However, band level, pair-wise comparisons showed significant differences ($p < 0.001$) in reflectance for each band, with Sentinel-2A exhibiting higher reflectance values than the HSI for the first three dates. Only for the last date (June 23rd) did the airborne HSI have higher reflectance values or no significant difference with the Sentinel-2A data. Overall, our three datasets captured the short-term phenological changes at Mer Bleue and have provided promising results in terms of using the Sentinel-2A MSI sensor to monitor these changes at the landscape level.

1. Introduction

Northern peatlands are a major ecosystem owing to their large extent (3% of Earth's surface) (Maltby and Immirzi, 1993), carbon storage capability over time (Gorham, 1991; Yu, 2012), and their role in the planet's climate regulation (Frolking et al., 2011; Maltby and Immirzi, 1993). In addition, peatlands provide important ecosystem services such as plant products (Chapman et al., 2003), host a unique array of biodiversity (Calmé et al., 2002) and have recently been recognized for their potential in mitigation strategies through their restoration (Leifeld

* Corresponding author.
E-mail address: juanpablo.arroyo-mora@nrc-cnrc.gc.ca (J.P. Arroyo-Mora).

https://doi.org/10.1016/j.rse.2018.07.021
Received 24 August 2017; Received in revised form 30 April 2018; Accepted 14 July 2018
Available online 24 July 2018

and Menichetti, 2018). From an understanding of their biogeochemical processes to potential changes due to climate change (Bellisario et al., 1999; Frolking et al., 2011), and their high degree of exploitation and degradation (Leifeld and Menichetti, 2018), northern peatlands present a significant challenge for forecasting their future contribution to the global carbon cycle (Gorham, 1991; Moore et al., 1998). For instance, at large spatial scales (hundreds of ha) current national and global scale datasets have been shown to underestimate their extent (Krankina et al., 2008). At medium scales (e.g. single peatland areas), peatlands are exceedingly difficult to accurately map because of their complex spectral properties (Kalacska et al., 2015) and poor accessibility (Harris et al., 2015). Finally, at local scales, peatland ecosystems fundamentally possess a fragile surface structure (i.e. mosses with interspersed vascular plants) that limits the establishment of representative field plots for in-situ measurements and monitoring.

In peatlands, carbon sequestration is controlled in part by the surface structure (i.e. vegetation composition) (Belyea and Malmer, 2004), which is inherently related to hummock-hollow-lawn microtopographic elements and the proportion of vascular plants and mosses these elements comprise. Hummocks are drier elevated mounds dominated by a vascular plant overstory than lower lying, wetter hollows, which are dominated by mosses (in bogs, generally *Sphagnum* spp.) (Eppinga et al., 2008). The vertical variation in elevation between hummocks and hollows is generally < 1 m (Lafleur et al., 2005). Vegetation characterization and dynamics studies in peatlands, aimed at identifying potential climate change effects (e.g. sink or source of greenhouse gases) (Moore et al., 1998; Tarnocai, 2006), require methodological approaches that can quantify the vegetation's structural and compositional variability across different spatial and temporal scales. Thus, the spatial scale must include 'plot to landscape' level measurements that can capture the spatial heterogeneity of the vegetation (Kalacska et al., 2015), while the temporal scale must be able to capture short term (e.g. monthly) to long term (e.g. decadal) variations (e.g. phenological changes). However, capturing vegetation composition at increasing spatial scales (e.g. from cm to km) is a major challenge in northern peatlands given their structural complexity (Harris and Bryant, 2013; Kalacska et al., 2015). In-situ spectral measurements have the potential for the characterization of hollows and hummocks, in terms of their structure and seasonal phenological changes. However, given the fragile surface structure of peatlands, representative sampling based on in-situ measurements is limited. Airborne HSI with very high spatial and spectral resolutions (e.g. ≤1 m) is another potential tool for assessing plant composition and phenological changes in peatlands. However, the cost and operational challenges of multiple airborne missions could be daunting, especially when covering large areas. Lastly, newer medium spatial and spectral resolution spaceborne platforms such as Landsat-8 OLI and Sentinel-2 (MSI instrument), might be limited in detecting vegetation characteristics at higher spatial scales (≤10 m) but may be able to capture general short-period phenological changes at the landscape level due to their high revisit time.

Remote sensing methods have been shown to provide promising peatland data at different spatial and spectral scales, and have become a suitable alternative to in-situ measurements of fragile peatland ecosystems (Harris and Bryant, 2013; Sonnentag et al., 2007). For instance, their utility ranges from the development of thematic maps from medium (> 10 m and < 30 m) spatial resolution satellite imagery for quantifying vegetation extent (Krankina et al., 2008; Poulin et al., 2002), to modeling foliar pigments using field spectroscopy and airborne hyperspectral imagery (HSI) at very high spatial and spectral resolutions (≤1 m) (Kalacska et al., 2015). However, a less explored venue in remote sensing of northern peatlands is the synergistic use of multiple data sets (Harris and Bryant, 2013) for validating satellite land products. The use of multiple remotely sensed datasets for validating land products (e.g. phenology, LAI, surface temperature) in peatlands is challenging, because ideally, it requires near-coincident spatial and temporal data as changes in vegetation characteristics happen over short periods of time. Multiple remote sensing data sets require different collection methodologies, which are time consuming and expensive. Moreover, to provide a direct comparison between datasets, post processing procedures (i.e. georectification, radiometric calibration, atmospheric correction) require high levels of expertise (i.e. consistent field spectroscopy measurements, hyperspectral airborne calibration/validation, radiometric and atmospheric corrections, etc.).

In this study, we have taken advantage of unique remote sensing datasets collected between April and June 2016 from the Mer Bleue Arctic Surrogate Simulation Site (MBASSS) Sentinel-2/Landsat 8 Data Product Validation Project (Soffer et al., 2017), which included near coincident field spectroscopy data (plot level), atmospherically corrected airborne VIS/NIR CASI-1500 HSI and Sentinel-2A MSI satellite imagery (Drusch et al., 2012). By implementing a bottom-up approach (from in-situ spectral characterization to satellite imagery), we use the plot level field spectroscopy data to evaluate the capability of the airborne HSI to capture the phenological trends for part of the growing season at Mer Bleue. Then, we resampled the airborne HSI to Sentinel-2A spectral and spatial characteristics and compared the temporal spectral variation for both image products using bottom of the atmosphere reflectance derived spectral vegetation indices. Thus, our overall objective was to identify key spectral features for assessing phenospectral dynamics (i.e. spectral changes as a function of vegetation phenological changes) for different vegetation physiognomies over a range of spectral, spatial and temporal scales at the Mer Bleue peatland. Furthermore, a novel aspect of our study is the evaluation of Sentinel-2A imagery for detecting phenological changes at the landscape level in a peatland area. More specifically, we addressed the following questions: 1: What are the main spectral features of the different vegetation physiognomies at the Mer Bleue peatland based on field spectroscopy? 2: How consistent are the spectral features of the different vegetation physiognomies at the Mer Bleue peatland when comparing resampled ground spectroscopy and airborne HSI? 3: How do ground reflectance and spectral indices at the Mer Bleue peatland compare between Sentinel-2A and airborne HSI? To the best of our knowledge, this is the first study that uses Sentinel-2A imagery in a northern peatland to assess seasonal phenological changes by integrating field spectroscopy and airborne HSI. This assessment is of great value for current and future land product validation efforts using satellite platforms.

2. Methods

2.1. Study area

This study was carried out at the Mer Bleue Conservation Area (MBCA) located east of the City of Ottawa, Ontario, Canada (Fig. 1). The MBCA is a 2800 ha ombrotrophic bog (i.e. water and nutrients come from precipitation and deposition as opposed to telluric sources) with hummock-hollow-lawn microtopographic features, poor fen sections, and beaver ponds around its margins (Moore et al., 2011). The climate of the region is cool continental, with a 30-year (1971–2000) mean annual temperature of 6.0 ± 0.8 °C. According to Roulet et al. (2007), the mean annual precipitation at Mer Bleue is 943 mm, of which approximately 235 mm falls as snow generally between December and March. In addition, the total precipitation is fairly evenly distributed throughout the year, with a minimum of 58 mm in February and a maximum of 90 mm in July.

The elevation for Mer Bleue is approximately 73 m ASL. The bog is slightly domed, with a peat depth increasing from 0.3 m along the edge to > 5 m across most of the area. Within the MBCA, the Mer Bleue Research Observatory (MBRO) is a long-term research site located in the northwest section (Fig. 1a). The MBRO covers approximately 10 ha and encompasses a series of boardwalks that allow for the implementation of field measurements of various types (e.g. gas exchange chambers, eddy covariance tower, field spectroscopy). For this study, we selected 5 vegetation physiognomic classes based on areas

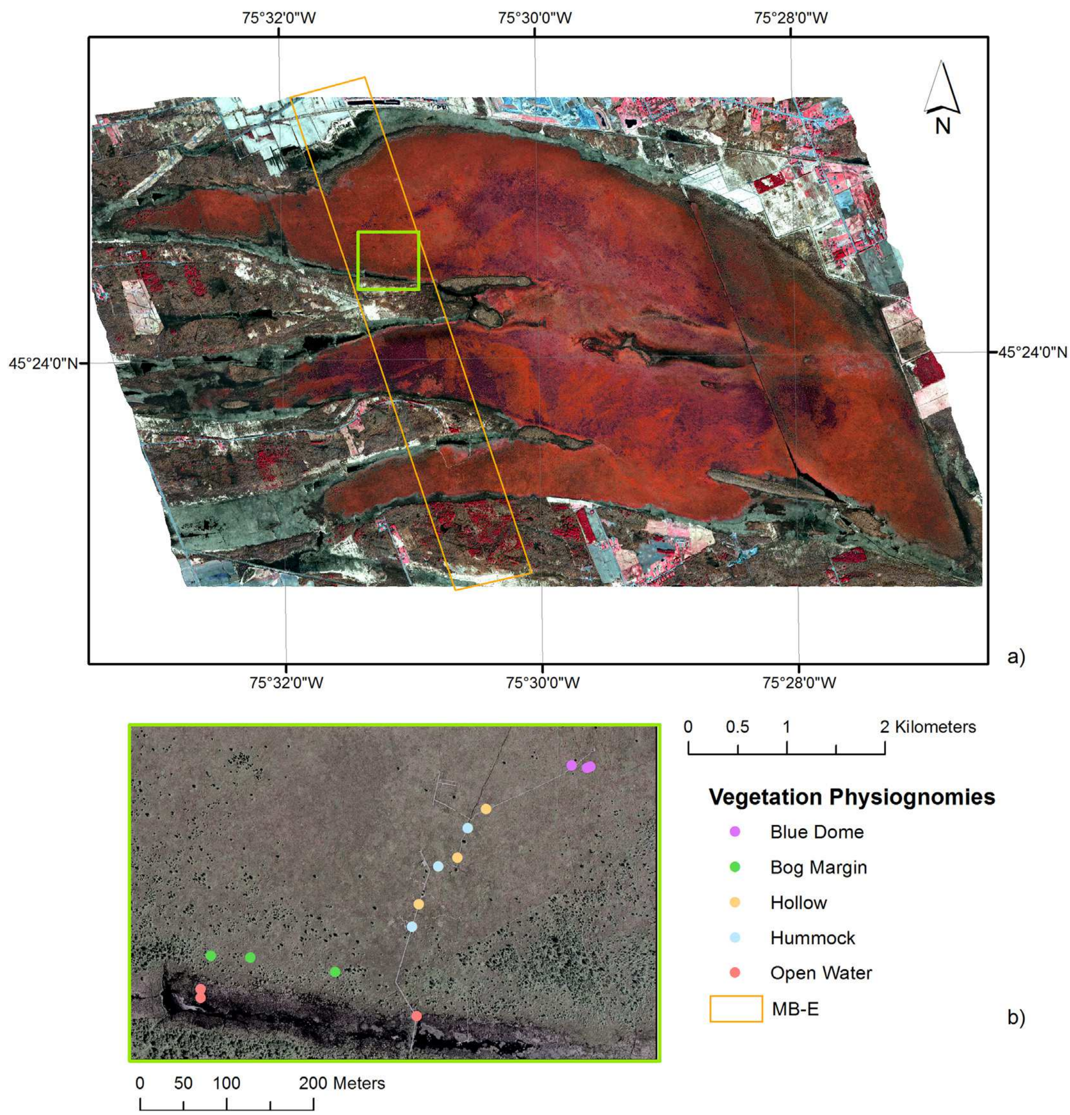

Fig. 1. HSI mosaic (CASI1500 imagery) of the Mer Bleue Conservation Area from April 20th, 2016 consisting of 12 individual flight lines (a). Flight Line E over the study area is highlighted in orange (MB-E). Insert shows an orthophoto (Source: Ottawa Orthophotos, 2005) for the Mer Bleue Research Observatory (MBRO) with the location of the vegetation plots (b).

Table 1
Vegetation physiognomic classes used to assess phenospectral changes from April to June 2016 using field spectroscopy and airborne hyperspectral data at the Mer Bleue Peatland Observatory.

Class	Description
Open Water	Exposed water in the beaver pond. Main species include *Sphagnum majus* and *Typha latifolia* (cattail).
Bog Margin	Area adjacent to the pond margin (transitional area from open water into grasses) located at the edge of the bog. In the bog margin, the deciduous herbs *T. latifolia*, *Calla palustris* and *Eleocharis smallii* are common.
Hummock	Hummocks account for approximately 51% of the peatland, and are primarily composed of *Sphagnum* sp. mosses, with shrubs up to 30 cm tall growing above the moss. In these areas *S. capillifolium* is most common, however very little moss is exposed.
Hollow	Hollows are composed of different types of *Sphagnum* spp. mosses, and are where most of the *Eriophorum vaginatum* (cotton grass) and other herbs primarily grow. In these areas the mosses *S. angustifolium*, and *S. fallax* are most common.
Blue Dome	This area contains mainly *S. magellanicum*, with fewer vascular plants.

accessible to field spectroscopy measurements at the MBPO (Fig. 1, Table 1). Physiognomic classes are defined here as the morphological characteristics of the vegetation; the horizontal and vertical vegetation structure, and species composition at a scale of 1 m. Detailed species composition characteristics can be found in Moore et al. (2011) and Kalacska et al. (2015).

2.2. Multi-data acquisition: general considerations

Near coincidental field spectroscopy plot level data, airborne HSI and Sentinel-2 imagery data aiming to capture phenospectral changes during part of the growing season at Mer Bleue was acquired for four dates: April 20th, May 11th, May 24th and June 23rd, 2016. The

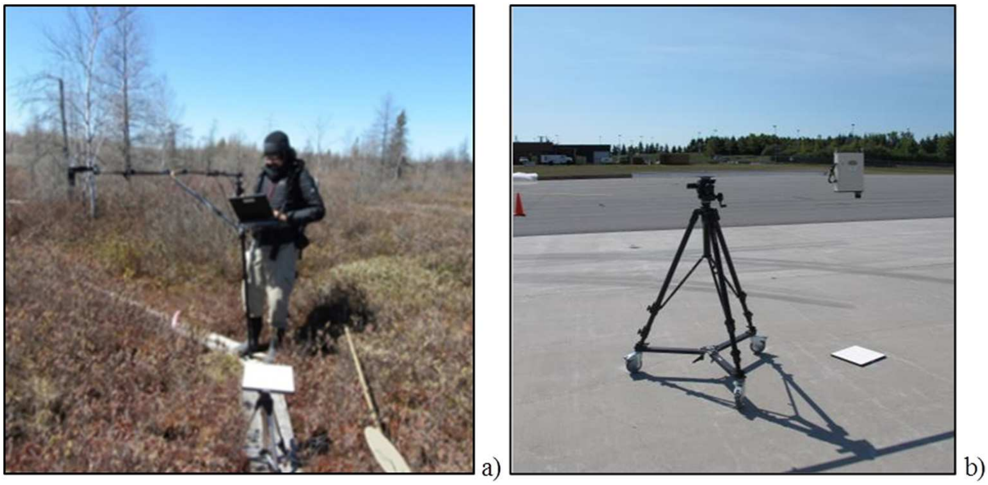

Fig. 2. Field spectroscopy (ASD FieldSpec3) setup for vegetation physiognomic class spectral characterization at Mer Bleue Research Boardwalk (e.g. bog margin plot) (a). Set up for concrete and asphalt target measurements at cal/val site using an SVC HR1024i spectroradiometer (b).

potential days for data collection, featuring clear atmospheric conditions with no or minimal cloud cover, were carefully determined based on meteorological forecasts.

For the analysis encompassing both the field spectroscopy data (field-spec, 15 plots) and the HSI, a subset of a single flight line was used (MB-E), since field data collection was restricted to boardwalk access at the MBRO. The comparison between the HSI with Sentinel-2A was conducted for the entire Mer Bleue peatland (Fig. 1).

2.3. Field spectroscopy acquisition and data processing

Fifteen field plots were established to cover the five physiognomic vegetation classes (Table 1). Each plot was recorded with a < 3 m horizontal error with a Garmin 60CSx GPS (Fig. 1). To measure the spectral reflectance of the vegetation physiognomies, an ASD FieldSpec 3 spectroradiometer (Analytical Spectral Devices Inc., Boulder, CO) with a 2 m fibre extension and 8° field of view (FOV) lens was used. The narrow boardwalks only allowed the use of a monopod with a perpendicular mechanical arm to hold the fibre optic, while the spectrometer was mounted in an operator worn backpack (Fig. 2a). To measure the same area consistently during the growing season, a mark was painted on the boardwalk, flagged, and an azimuth was determined. Measurements were then taken over the same area as consistently as this set up permitted. The use of the monopod arm and fibre extension also provided separation between the operator and the target, to minimize errors that result due to operator induced influences (Kimes et al., 1983). The vertical separation between the 8° FOV fore-optics and the target location on the ground was approximately 1.6 m, which resulted in a 22 cm diameter sample spot size. The restriction of the 25° bare fibre FOV by the 8° fore-optics was necessary as the Spectralon™ panel deployed in the field had a width of 25.4 cm. The field spectrometry consisted of a measurement of a calibrated Spectralon™ reference panel followed by measurements of the vegetation plot (3 repetitions, each averaging 25 scans), a second measurement of the reference panel and a final panel measurement under shadowed conditions, in order to determine the diffuse versus global irradiance conditions. Target reflectance was calculated from the ASD measurements, via a panel substitution methodology, which compares a measurement of the target of interest with that of a target of known reflectance (i.e. Spectralon ™ panel) using Eq. (1).

$$R_T(0^{\circ}, \phi_i) = \frac{\frac{S_T(\theta_{iT})}{Cos(\theta_{iT})}}{\frac{S_R(\theta_{iR})}{Cos(\theta_{iR})}} \times RF \tag{1}$$

where R_T is the reflectance of the target (e.g. open water plot) with viewing angle at 0° and an illumination angle of ϕ_i. S_T and S_R are the measured signals from the ASD of the target and reference panel respectively, and θ_{iT} and θ_{iR} are the solar zenith angle at the time of the target and reference measurements. Lastly, RF is the reflectance factor of the panel taking into consideration a first-order correction of the 8°: hemispherical reflectance factors provided with a new panel to the 0°:45° biconical reflectance viewing and illumination geometry factors of Spectralon™ (Yoon et al., 2009; Williams, 1999). Photographs of each plot were taken along with each measurement to aid interpreting the vegetation changes throughout the growing season (Appendix A1).

Additional ground spectra of concrete and asphalt targets were collected at NRC-FRL's calibration/validation (cal/val) site located at the Ottawa International Airport coincident with the HSI acquisition in order to improve the atmospheric correction (described below). These cal/val spectra were collected with an SVC HR1024i spectroradiometer (Spectra Vista Corporation, Poughkeepsie NY). The spectrometer head was fixed to the end of an extension arm mounted to a video camera tripod at a height of 1.4 m (Fig. 2b). A 4° FOV fore-optic resulted in a sample spot size of approximately 10 cm. Target reflectance was calculated as described above with Eq. (1). A cross calibration between the two instruments and Spectralon™ panels used in the field at Mer Bleue and at the cal/val site showed a consistency of 1% across the wavelength range.

2.4. Airborne hyperspectral imagery (HSI) acquisition and processing

For the collection of the airborne hyperspectral data, a Compact Airborne Spectral Imager-1500 (CASI-1500) grating-based, push-broom imager (silicon frame transfer charge coupled device sensor) was used (Table 2). The instrument was mounted in a Twin Otter aircraft operated by the National Research Council Canada's Flight Research Laboratory (NRC-FRL). To cover the entire MBCA, 12 parallel flight lines were required, each with a nominal image swath width of 800 m, based upon an aircraft altitude of 1103 m AGL and 20% overlap between flight lines. The CASI is programmable with up to 288 spectral channels (2.4 nm spacing, 3.2 nm resolution) for each spatial pixel. The full 288

Table 2
Summary of key operation characteristics of the CASI-1500 HSI.

Characteristic	Value
Spectroradiometric calibration	March 26th, 2015
Geometric bundling calibration	May 6th, 2015
No. cross-track pixels (detector)	1500
No. cross-track pixels (image)	1498
FOV (°)	39.83
Instantaneous FOV (°)	0.0277 (nadir)
	0.0245 (edge)
No. bands	288 (selectable)
Spectral range (nm)	366–1053
Spectral resolution (nm)	3.2
Frame rate (frames/s)	Programmable – max rate depends on # of bands.
	144 bands @ 40
	288 bands @ 23
Integration time (ms)	1000/frame rate
Focal length (pixels)	2067.36

spectral channel configuration was used in the HSI acquisition.

Each flight line was spectroradiometrically corrected following methods established by Kalacska et al. (2016), which includes a correction of the spectral alignment, removal of signal offsets for each pixel and a smile correction. The radiometrically corrected images were then atmospherically corrected using ATCOR 4.7.0 (Richter and Schläpfer, 2002). To remove spectral residual atmospheric artefacts, a vicarious calibration was carried out based on two targets (concrete and asphalt) at the cal/val site and subsequently applied to each flight line (Brook and Dor, 2011; Secker et al., 2001; Teillet et al., 2001). The cal/val site (45.32° N, −75.67° W) is approximately 14 km SW of Mer Bleue. Flight lines were flown over both sites on the same day, with similar atmospheric conditions. Following vicarious calibration for both asphalt and concrete, the spectral reflectance across the wavelength range was within ± 2% of the ground spectra.

In order to create a full mosaic for each sampling date, each set of the 12 flight lines was subsequently geocorrected and mosaicked with the 'minimize view zenith angle' option to select which of the duplicate pixels located in the overlap between adjacent flight lines are applied in the resulting mosaic imagery (ITRES, 2013). During geocorrection, all HSI flight lines were resampled to 1 m pixel size. Of the original 288 bands, 175 bands were retained to be equivalent to the Sentinel-2A spectral range (450.52–866.59 nm).

2.5. Sentinel-2 processing

Four Sentinel-2A images (with minimal to no cloud cover) were retrieved from the USGS Earth Explorer archives. The images were obtained at Level 1C: Top of the Atmosphere (TOA) reflectance (ESA, 2016). To produce Level 2A Bottom of Atmosphere (BOA) reflectance products, these images were processed using Sen2cor 2.2.1 (Müller-Wilm, 2016), resulting in four reflectance images at 20 m spatial resolution with 9 spectral bands. The 9 bands correspond to three 10 m channels resampled by Sen2cor 2.2.1 to 20 m (B2, B3, B4), and the six 20 m bands (B5, B6, B7, B8A, B11 and B12) (Fig. 3). After careful review of the reflectance data (i.e. calculated BOA), it was found that the central wavelengths in the ESA (2016) report did not correspond to the actual central wavelengths reported in the metadata of the BOA images (i.e. xml file). Due to this difference, the central wavelengths used for the data products were calculated from the BOA metadata (Fig. 3). An example of this discrepancy was found in Band 2 and Band 12, where the difference between reported and metadata central wavelengths are 6.6 nm and 12.4 nm, respectively, while Band 8A indicates a difference of 6.9 nm.

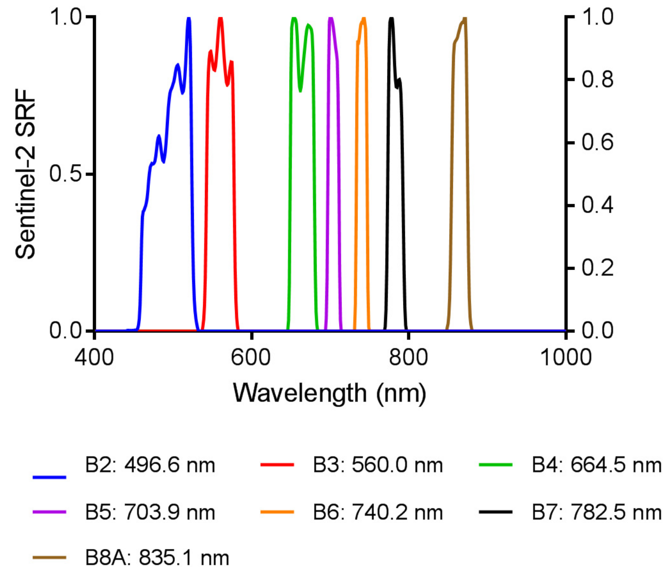

Fig. 3. Spectral response for the Sentinel-2A Multispectral Instrument sensor (modified from ESA, 2016). Only the first seven bands that correspond to the wavelength range of the airborne HSI (CASI-1500) are shown.

2.6. Data preparation

Because the overall goal of this study was to evaluate the utility of Sentinel-2A to assess phenological changes at Mer Bleue supported by field spectroscopy and airborne HSI, the first assessment comparing the field spectroscopy (350–2500 nm) with the airborne HSI reflectance data was done using the 450.52 nm to 866.59 nm region, which corresponds to bands 2-8A of Sentinel-2A. Three steps were necessary to select pixels across the HSI's FOV that were consistent with the spatial locations of the 15 field plots. First, the flight line MB-E was clipped to the area of the vegetation plots (Fig. 1B). Despite having been georeferenced, offsets of approximately 2 pixels (2 m) between the flight line E images from different collection dates were observed in some areas. As a result of the offset, a further geocorrection of the clipped subsets was carried out using a semi-automatic image to image geocorrection (1st order polynomial) in ENVI 5.3. The April 20th image was used for the geocorrection of the May 11th and May 24th (RMSE errors of 0.8 and 1.08 m, respectively), while the June 23rd subset was georeferenced to the May 24th subset (RMSE = 0.9 m).

Next, we used a 2 cm spatial resolution UAV derived RGB orthomosaic to improve the localization of the field plots corresponding to the correct pixel in the HSI data. By spatially overlaying each one of the HSI subsets on the RGB image with the plot location, we were able to select pixels in the four HSI datasets that corresponded to the field spectra plot measurements. We used well-defined coincident features in both the HSI and the RGB images, such as the boardwalk, to assess the accuracy of the pixel selection. In addition, we also considered not only the position of the pixel but also the azimuth (recorded in the field) of the ground plot locations with respect to the boardwalk. Once the pixels were selected, the reflectance spectra were extracted and averaged by physiognomic class for each plot. These physiognomic class spectra were then organized in a spectral library for further analysis.

For the spectral comparison between the Sentinel-2A and the HSI mosaics, the four HSI mosaics (Fig. 4) were spatially and spectrally resampled to the Sentinel-2A images (accounting for Sentinel-2A response functions). The result of this re-sampling was four HSI datasets at 20 m spatial resolution with the same band set as that of the coincident Sentinel-2A reflectance image. We used the MBCA full mosaic

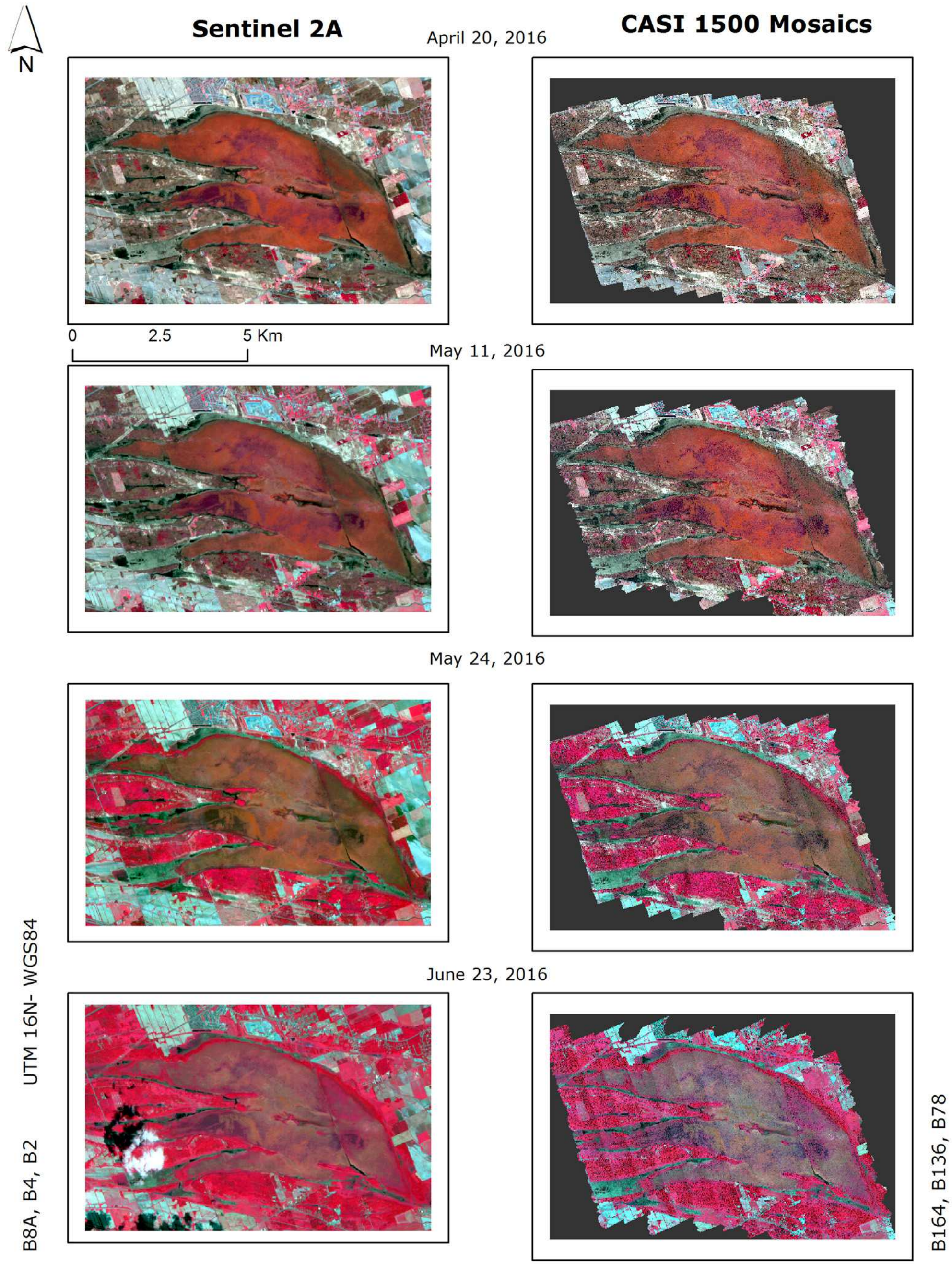

Fig. 4. Sentinel-2A satellite images (left) and airborne HSI (CASI-1500) mosaics (right) for Mer Bleue Conservation Area. The projection for both datasets is UTM 18 N, WGS4. Band combination for Sentinel 2A corresponds to B8A: 853.1 nm, B4:664.5 nm and B2: 496.6 nm. Band combination for the airborne HSI mosaic corresponds to B164: 756.6, B136: 689.7 nm and B78: 550.9 nm.

that encompassed nearly the same area as the satellite image. In order to carry out the comparison between the airborne HSI and the Sentinel-2A imagery, 20 1-ha plots (5 × 5 pixels) were randomly selected over the entire MBCA (Fig. 5).

2.7. Data analysis

To assess the overall differences in spectral shape and amplitude between the field spectroscopy and the HSI for the different vegetation physiognomies over time, we used the θ (amplitude) and D (shape) metrics (Price, 1994) (Eqs. (2) and (3), respectively).

$$\theta = \cos^{-1}\left[\frac{\int S_1(\lambda)S_2(\lambda)d\lambda}{[\int S_1(\lambda)d\lambda]^{\frac{1}{2}}[\int S_2(\lambda)d\lambda]^{\frac{1}{2}}}\right] \tag{2}$$

$$D = \left[\frac{1}{\lambda_b - \lambda_a}\int_{\lambda_a}^{\lambda_b}[S_1(\lambda) - S_2(\lambda)]^2 d\lambda\right]^{1/2} \tag{3}$$

where $S1$ and $S2$ are pairs of spectra over a wavelength range (λ_a–λ_b).

An initial visual assessment of the differences between the field and the HSI spectra for each vegetation physiognomy revealed a greater similarity between the data sets in the visible range (450–680 nm)

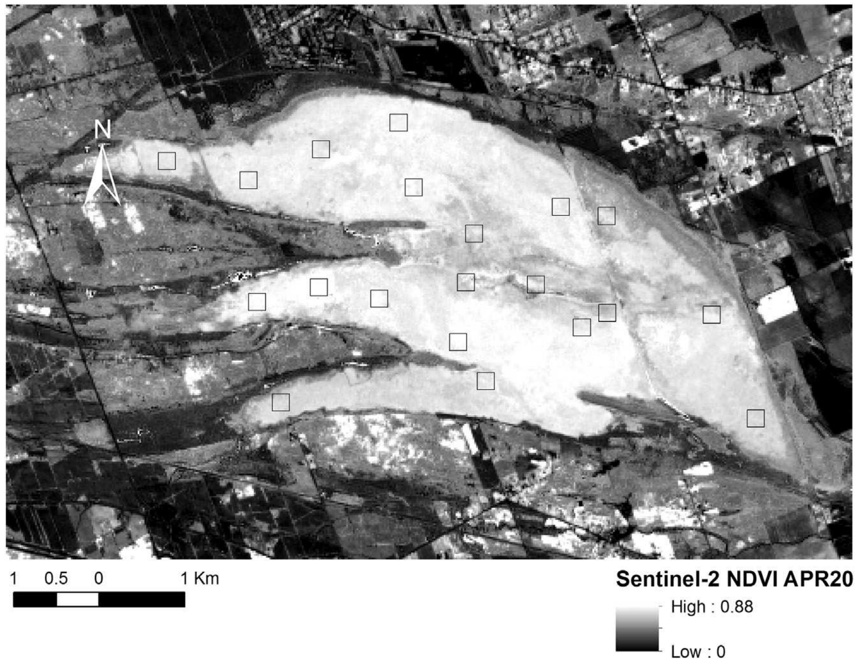

Fig. 5. Random distribution of 1-ha plots (5 × 5 pixels) used to extract reflectance and vegetation index values from Sentinel-2A and resampled CASI-1500 mosaics. Base image illustrates NDVI from April 20th, 2016.

compared to the near infrared range (681–866 nm), therefore, the spectra were divided into the aforementioned spectral ranges in order to calculate θ and D.

We applied continuum removal (Kokaly et al., 2003) to the field spectra and the HSI reflectance to identify the main spectral features for each vegetation physiognomy. Furthermore, we calculated the first and second derivatives of these spectra to clearly identify global and local regions of variation, as well as the rates of these changes. Overall, these methods were used to assess how consistent the spectra are over time (phenospectral changes), and between sensors.

The comparison between the Sentinel-2A and HSI resampled dataset (20 m resolution and 7 spectral bands) was based on the reflectance values from each data collection period as well as on three vegetation indices commonly used to measure vegetation dynamics in different ecosystems (Table 3). For each of the 20 1-ha plots (5 × 5 pixels), the average reflectance of the 25 pixels was calculated, and the mean reflectance was compared for each band using a *t*-Test (assuming unequal variances). In addition, a correlation analysis for each band between the resampled HSI and the Sentinel-2A imagery was performed using the same plots.

3. Results

Overall, the spectral signatures for the vegetation physiognomies at Mer Bleue show a good correspondence between the field spectroscopy (field-spec) and the HSI reflectance across the four dates (Fig. 6). For instance, only small spectral differences are found in the visible range (VIS: 450–680 nm) compared to larger differences in the near-infrared portion (NIR: 681–866 nm) (Fig. 6). Amplitude (D) results support this finding, with D values in the NIR being larger than the VIS range across vegetation physiognomies for the four dates (Table 4). D values in the VIS range from 0.16 for the blue dome (May 24th), to 1.41 for open water (May 11th), while for the NIR range, D values range from 0.38 (June 23rd) to 4.05 (May 11th) for open water. Spectral shape differences (θ), also indicate larger values in the NIR than the VIS spectral range (Table 4). In terms of the spectral variability, shown by the standard deviation for the field spectroscopy and HSI reflectance in Fig. 6, no distinct patterns were found. However, in general, the open water plots show larger standard deviations from the mean compared to the other physiognomic classes.

Results from the continuum removal reveal three absorption features that capture phenological changes characteristic of Mer Bleue (Fig. 7). The first feature encompasses the global minimum (lowest scaled reflectance value), corresponding to the red absorption well between 675 nm to 680 nm for the field spectra (Table 5) and from 668 nm to 682 nm for the HSI (Tables 5 and 6). The global minima for both field spectra and HSI are very similar (mode 678 nm and 677 nm, respectively), with < 3 nm differences across vegetation physiognomies and dates. Two exceptions are the bog margin class on April 20th (5 nm) and June 23rd (6 nm) and open water on June 23rd (8 nm). In addition, in both the field spectra and the HSI, the blue dome has the lowest reflectance from April 20th to May 24th. For June 23rd the lowest reflectance is seen for the bog margin (Fig. 7). First derivative results are consistent with the continuum removal results when

Table 3
Vegetation indices used to compare resampled HSI images and Sentinel-2A products.

Vegetation index	Formula (Sentinel-2 reflectance channels)	Reference
Normalized Difference Vegetation Index (NDVI)	$(NIR_{B8} - R_{B4}) / (NIR_{B8} + R_{B4})$	Rouse et al. (1974)
Single Ration (SR)	NIR_{B8} / R_{B4}	Birth and McVey (1968)
Red Edge Normalized Vegetation Index (RENDVI)	$(NIR_{B6} - NIR_{B5}) / (NIR_{B6} + NIR_{B5})$	Gitelson and Merzlyak (1994)

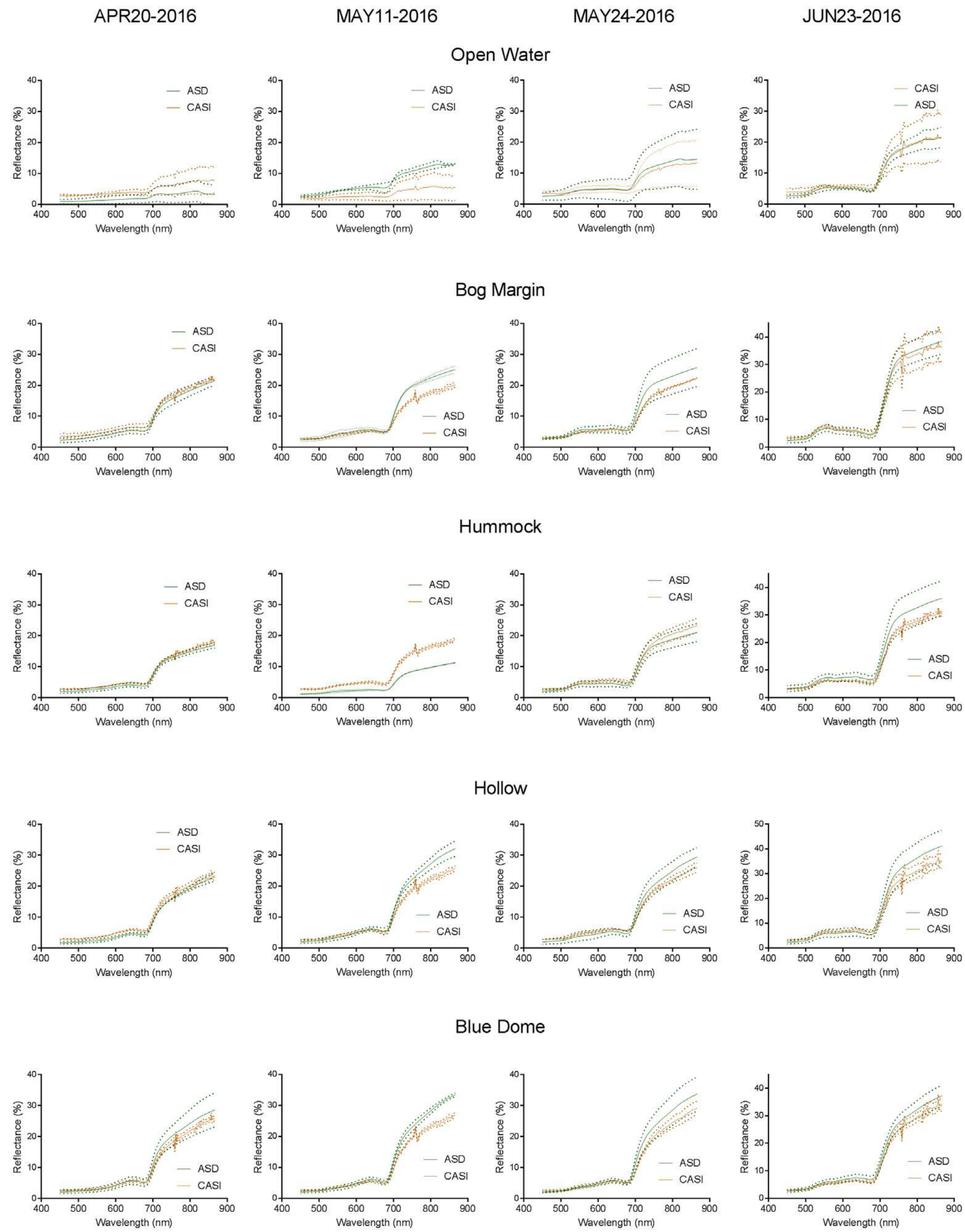

Fig. 6. Field spectroscopy (ASD) and HSI (CASI1500) spectral reflectance for four dates encompassing part of the phenological cycle (i.e. vegetation greening) at the Mer Bleue Peatland Observatory in 2016.

determining the global minima for the field spectra and the HSI reflectance (Tables 5 and 6). However, the difference in the location of the minima between the continuum removal and the 1st derivative is smaller in the field spectra across than for the HSI across vegetation physiognomies and dates. Excluding the open water plot for April 20th, the difference in the location of the global minima between the continuum removal and the 1st derivative ranges from 3 nm to 7 nm (mode 4 nm). In terms of the inflection point results based on the 2nd derivative, we found a larger difference between inflection points on either side of the green peak for the field spectra than the HSI across vegetation physiognomies and dates (Tables 5 and 6).

A second spectral feature (local maximum) located in the red region approximately between 600 and 650 nm is noticeable in the field spectra and the HSI reflectance for April 20th, especially for the blue dome and hollows (636 nm) and is less evident for the bog margin and hummocks (606 nm and 610 nm, respectively) (Fig. 7a–b). This spectral peak is still captured in the May 11th field plot reflectance but becomes less apparent in the HSI (Fig. 7c and d, respectively). In this red region, for the field plots, phenospectral changes reveal a shift from the approximate center of the absorption feature at 635 nm (April 20th and May 11th) to the lower left boundary of the feature at 600 nm (May 24th and June 23rd) for the blue dome and the hollows which are moss dominated (Fig. 8a, c). However, for the same absorption feature, the bog margin and hummocks show a negligible phenospectral change. Comparatively, the red region absorption feature in the HSI data is not seen for the hummock class and becomes imperceptible after May 11th for the blue dome, bog margin and hollows (Fig. 8b, d).

The third spectral feature is located in the green region between

Table 4
Spectral amplitude (D) and shape (θ) comparison between field-spec and HSI spectral reflectance (Fig. 6) at two spectral ranges for four dates during the first half of the 2016 phenological cycle at the Mer Bleue Peatland Observatory. BD: Blue dome, BM: Bog margin, HO: Hollow, HU: Hummock and OW: Open Water.

	Visible (450–680 nm)							
	20-Apr		11-May		24-May		23-Jun	
	D	θ	D	θ	D	θ	D	θ
BD	0.26	0.0867	0.22	0.0777	0.16	0.0527	0.43	0.0611
BM	0.51	0.0904	0.21	0.0516	0.24	0.0589	0.38	0.0515
HO	0.29	0.0998	0.24	0.0845	0.47	0.0470	0.50	0.0544
HU	1.19	0.0888	1.28	0.0495	0.48	0.0666	0.65	0.0520
OW	1.31	0.1371	1.41	0.1463	0.26	0.0727	0.54	0.0808
	NIR (681–866 nm)							
BD	3.68	0.0281	3.09	0.0345	2.44	0.0205	1.68	0.0291
BM	1.81	0.0420	2.85	0.0335	2.16	0.0295	0.96	0.0289
HO	3.92	0.0383	2.97	0.0367	1.59	0.0189	2.91	0.0311
HU	3.50	0.0286	3.92	0.0318	0.93	0.0247	2.85	0.0277
OW	2.10	0.1031	4.05	0.0494	0.87	0.02663	0.38	0.0309

525 nm to 575 nm (green peak). It is noticeable in the field spectra from May 11th to June 23rd (Fig. 7e–g) and in the HSI spectra only for May 24th and June 23rd (Fig. 7f–h). In addition, based on the field spectra, the blue dome shifted towards the peak of the green region (approximately 540 nm) only in the June 23rd data, while the bog margin increased from 528 nm to 544 nm between May 11th and May 24, and slightly decreased to 541 nm on June 23rd (Fig. 8c). Following April 20th, hollows shift on May 11th from 526 nm to 539 nm. On the other hand, phenospectral changes based on the airborne HSI data (Fig. 8b–d) have a less clear pattern for the vegetation physiognomies, with the exception of the bog margin where the peak reflectance shifted from 529 nm to 514 nm (Fig. 8d).

Results comparing the resampled airborne HSI mosaics and the Sentinel-2A reflectance product show very similar trends over time (Fig. 9). For instance, in the visible region both the resampled airborne HSI and Sentinel-2A reveal a distinct increase in the green peak at 560 nm (Band 3) from April 20th to June 23rd, 2016. In addition, an increase in the slope between 664.5 nm and 703.9 nm (red edge) is consistent for both products for the same period. However, although these trends are similar for both sensors, band level reflectance comparisons (Fig. 10) reveal significant differences for all bands and dates ($p < 0.0001$) with the exception of Band 6 on June 23rd. For instance, Sentinel-2A shows significantly higher reflectance values per band during the first three dates, while this pattern is reversed in some bands (B2, B3, B4 and B7) for June 23rd, exhibiting higher values from the HSI resampled data. Band correlation results between Sentinel-2A and the resampled HSI (Fig. 11) show no apparent trend (r range between 0.129 and 0.731). In general, higher correlation values are found in red edge bands and higher correlation coefficient values are more distinct for May 24th (range 0.474–0.731).

Vegetation index results for the HSI mosaics and Sentinel-2A reveal differences between both sensors when capturing the phenospectral patterns at Mer Bleue. For instance, SR and NDVI values from April 20th to June 23rd increase for the CASI, however for Sentinel-2A, April 20th has higher SR and NDVI values than May 11th (Table 7, Fig. 12a–b). Then, from May 11th to June 23rd both the SR and NDVI values increase. Pair-wise comparisons indicate that SR and NDVI values are significantly different across dates within each sensor ($p < 0.0001$). Moreover, pair-wise comparisons for each vegetation index between sensors also reveal significant differences for each time period. RENDVI, from the CASI increases across all dates. On the other hand, for RENDVI from Sentinel-2A, there is no significant difference between April 20th and May 11th ($p > 0.78$). However, the increase in RENDVI from May 11th to June 23rd is statistically significant ($p < 0.0001$).

4. Discussion

Our remotely sensed data validation consisted of assessing whether different spatial and spectral near-coincident datasets captured short-term phenospectral changes in a peatland between April 20th and June 23rd, 2016. By implementing a bottom-up approach, we used in-situ field spectroscopy measurements to validate airborne hyperspectral data (HSI) at the local spatial scale (plot level). A previous study by Kalacska et al. (2015) at Mer Bleue showed the utility of ground spectra to characterize changes in foliar chlorophyll and nitrogen over a growing season. We then used the airborne HSI data to validate Sentinel-2A satellite imagery for the same time period over the entire MBCA. Broadband mid-resolution satellites have been used to assess phenological changes in multiscale studies in different ecosystems (Fisher et al., 2006; Reed et al., 2009), however, to our knowledge, this is the first study testing Sentinel-2A capabilities for assessing ecosystem processes (i.e. phenology) in a peatland, using near coincidental in-situ field spectroscopy and HSI data.

Mer Bleue presents a mixed plant community composed of vascular plants and mosses, whose densities provide the structural characteristics of two of the main features in the peatland: hummocks and hollows (Lafleur et al., 2005). Our field spectroscopy data captured a FOV of approximately 22 cm, while the airborne HSI spatial resolution was approximately 1 m (from 1103 m AGL). Given that the FOV of the in-situ data capturing the vegetation is at a finer spatial scale, in most cases the field spectroscopy reflectance values are higher than the HSI (Fig. 6). However, amplitude differences between both spectral measurements are lower in the visible range than in the near-infrared for most cases (Fig. 6), which may indicate spectral homogeneity within pigments regardless of the vascular plant and moss densities. Changes in vegetation structure are more variable for the different vegetation physiognomies, which may be explained by the larger differences measured in the near-infrared region. Phenospectral vegetation response based on continuum removal and first derivative analysis during the April 20th to June 23rd time period further show that these changes are consistent between field spectroscopy measurements and airborne HSI, even when considering narrow spectral features (Tables 5 and 6). For instance, the global minima for both spectral measurement results show the well-known chlorophyll absorption feature between 660 and 680 nm (Sims and Gamon, 2002) (Fig. 7). This absorption feature slightly increased from April to June, which is explained by changes in chlorophyll absorption as plants green up, and is consistent with a strong spectral feature found at the 525–575 nm spectral range (green peak). In this peatland, after the snow melt in mid to late April, spring growth has not yet started and vegetation mostly resembles the senescent period (brown and reddish tones), which is captured by the 600–640 nm range peak, especially for hollows and the blue dome vegetation physiognomic classes. As the vegetation starts greening up during early May, there are subtle differences between vascular plants (i.e. herbs and shrubs) and mosses that drive small variations in reflectance. Kalacska et al. (2015) found an increase in the concentration of total chlorophyll dominated by vascular plants for the same phenological period, while the mosses showed less temporal variability.

At the landscape level (i.e. MBCA), both airborne HSI and Sentinel-2A reflectance are very consistent in capturing the greening of the Mer Bleue peatland, as indicated by the increase in reflectance from April to June in both datasets at 560 nm (Fig. 9). In addition, changes in vegetation structure, likely driven by changes in leaf area index (LAI) for

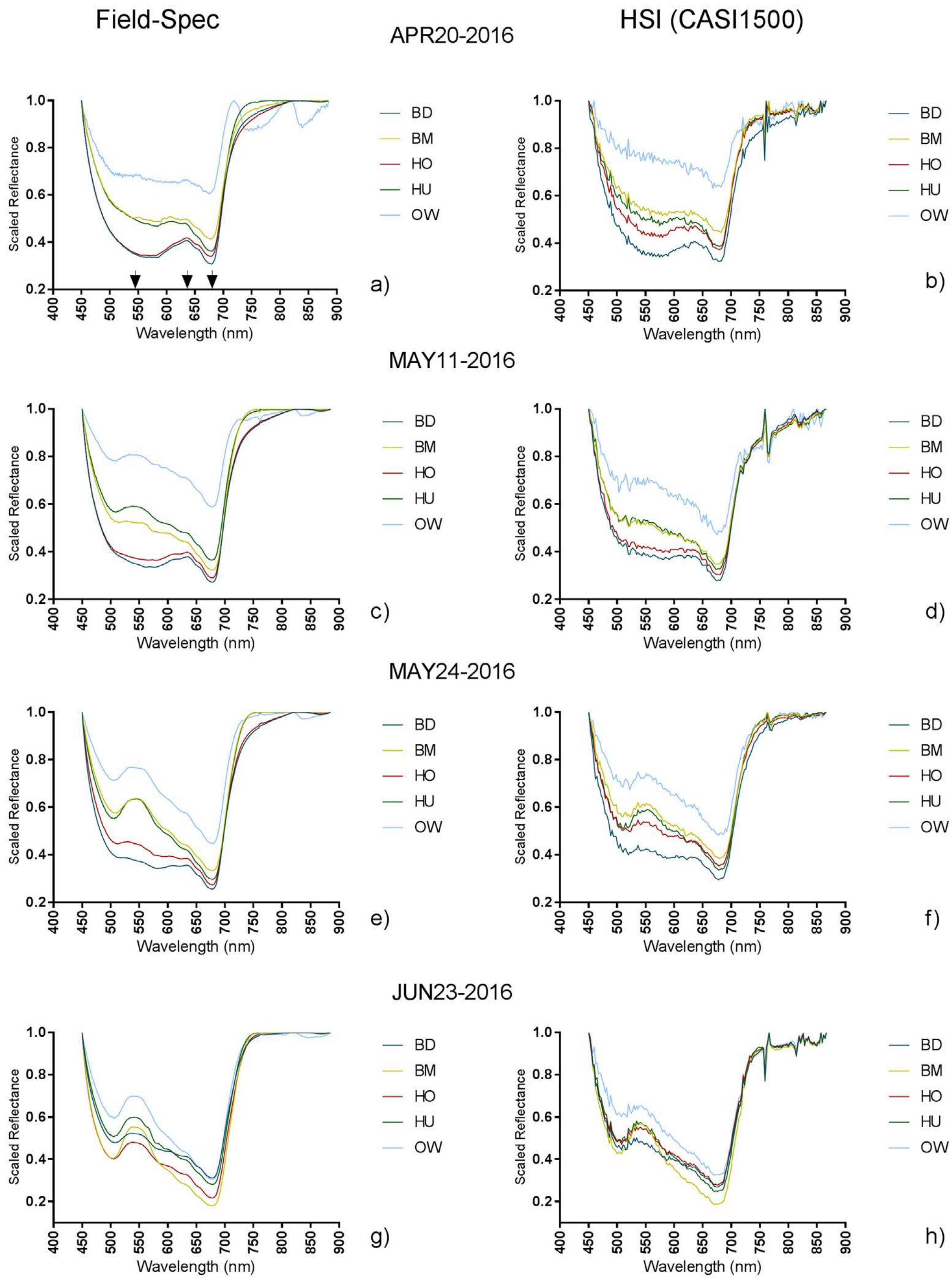

Fig. 7. Continuum removal scaled reflectance for the field spectroscopy (Field-Spec) and the HSI (CASI-1500) spectra for the 5 vegetation physiognomic classes for the four dates at Mer Bleue. BD: Blue dome, BM: Bog margin, HO: Hollow, HU: Hummock and OW: Open Water. Black arrows in (a) represent the main absorption features revealing phenospectral changes for the different dates. (For interpretation of the references to colour in this figure legend, the reader is referred to the web version of this article.)

hummocks (as vascular plants green up), are evident as both datasets indicate an increase in reflectance of the red edge and the amplitude of the near infrared region (this pattern is also captured by the field spectroscopy data). LAI of shrubs increases partly from the deciduous *Vaccinium myrtilloides* for example, but also there is a substantial increase for the evergreen shrubs (e.g. *Chamaedaphne calyculata*).

The identification of short-term phenological changes is important in peatland areas because these changes are related to hydrological and biogeochemical cycles. For instance, the annual carbon budget is controlled in part by the onset of spring photosynthesis and carbon uptake (Moore et al., 2006). A complex interaction between micro-topography, water table depth, peat temperature in the rooting zone and species composition is reactivated at Mer Bleue after the snow melts and moss species become active, followed by the greening of vascular plants and leaf development in deciduous species. Moreover, according to Moore et al. (2006), although there is evidence of warmer springs around the Mer Bleue peatland (increase of 0.21 °C per decade between 1939 and 2004), this might not have a profound effect on the

Table 5
Continuum removal, first and second derivatives for field plot based spectra. BD: Blue dome, BM: Bog margin, HO: Hollow, HU: Hummock and OW: Open Water.

ASD plots	Cont. rem local min. (nm)	Refl. local min. (nm)	1st der. local min. (nm)	1st der. refl. local min. (nm)	2nd der. infl. point G-R (nm)	2nd der. infl. point V-NIR (nm)	Difference infl. points (nm)
APR20-BD	679	0.31	674	0.51	659	731	72
APR20-BM	677	0.42	673	0.53	670	740	70
APR20-HO	678	0.34	673	0.61	665	738	73
APR20-HU	680	0.36	673	0.37	651	742	91
APR20-OW	675	0.61	651	0.18	669	721	52
MAY11-BD	678	0.27	674	0.53	652	718	66
MAY11-BM	678	0.32	674	0.50	676	722	46
MAY11-HO	678	0.29	674	0.54	696	745	49
MAY11-HU	676	0.37	672	0.32	651	702	51
MAY11-OW	678	0.59	671	0.36	667	738	71
MAY24-BD	677	0.26	674	0.50	700	750	50
MAY24-BM	679	0.33	673	0.54	660	749	89
MAY24-HO	678	0.27	675	0.47	657	743	86
MAY24-HU	679	0.30	673	0.39	652	712	60
MAY24-OW	677	0.45	673	0.44	678	722	44
JUN23-BD	678	0.31	673	0.68	652	711	59
JUN23-BM	677	0.18	674	0.45	674	701	27
JUN23-HO	677	0.22	673	0.53	664	703	39
JUN23-HU	679	0.28	673	0.65	654	706	52
JUN23-OW	679	0.31	672	0.42	664	750	86

Table 6
Continuum removal, first and second derivatives for airborne HSI (CASI-1500). BD: Blue dome, BM: Bog margin, HO: Hollow, HU: Hummock and OW: Open Water.

ASD plots	Cont. rem local min. (nm)	Refl. local min. (nm)	1st der. local min. (nm)	1st der. refl. local min. (nm)	2nd der. infl. point G-R (nm)	2nd der. infl. point V-NIR (nm)	Difference infl. points (nm)
APR20-BD	677.74	0.32	673.08	0.48	692.09	742.29	50
APR20-BM	682.52	0.45	668.18	0.63	689.70	739.90	50
APR20-HO	680.13	0.37	668.18	0.55	670.57	720.78	50
APR20-HU	680.13	0.39	668.18	0.44	673.35	720.78	47
APR20-OW	677.74	0.32	668.18	0.37	677.74	727.95	50
MAY11-BD	675.35	0.28	668.18	0.48	692.09	742.29	50
MAY11-BM	680.13	0.35	670.57	0.48	682.52	732.73	50
MAY11-HO	680.13	0.30	673.08	0.51	694.48	744.68	50
MAY11-HU	672.96	0.33	673.08	0.43	658.61	708.82	50
MAY11-OW	675.35	0.47	675.35	0.23	663.39	713.60	50
MAY24-BD	677.74	0.30	677.74	0.51	649.04	699.26	50
MAY24-BM	680.13	0.39	670.57	0.54	665.79	715.99	50
MAY24-HO	677.74	0.35	668.18	0.56	663.39	713.60	50
MAY24-HU	677.74	0.34	668.18	0.50	658.61	708.82	50
MAY24-OW	677.74	0.48	668.18	0.46	654	704	50
JUN23-BD	675.35	0.27	670.57	0.57	677.74	727.95	50
JUN23-BM	670.57	0.19	670.57	0.47	677.74	727.95	50
JUN23-HO	675.35	0.28	668.18	0.63	675.35	725.56	50
JUN23-HU	675.35	0.25	670.57	0.51	675.35	725.56	50
JUN23-OW	670.57	0.33	668.18	0.50	675.35	725.56	50

annual carbon budget. Sentinel-2A reflectance products could provide a baseline and long-term phenology monitoring tool to test this hypothesis as well as other aspects related to climate change in northern peatlands.

Our results revealed that significantly higher reflectance values for most bands in Sentinel-2 compared to HSI mosaics for the first three dates (except Band 8A: 831.5 nm), but not for June 23rd, might be explained by sensor characteristics and subtle phenological changes (Fig. 10). For instance, although HSI mosaics were resampled to Sentinel-2A spectral and spatial resolutions, the higher radiometric resolution (14 bits) of the HSI compared to Sentinel-2A (12 bits) is likely to be retained in the resampling process. Therefore, while the HSI mosaics and the Sentinel-2A are comparable spatially and spectrally, the pixel information that the HSI mosaic captured (brightness values) is more detailed. In early spring, microtopographic elements in hollows (mosses dominant) and hummocks (vascular plants dominant) could produce shadow effects that are captured by the HSI sensor (lower reflectance values), but are less evident in the 20 m native pixel resolution of the Sentinel-2A sensor. For June 23rd, vegetation is homogeneously green in the peatland and the subtle microtopographic differences are less influential in the spectral response of the sensor. In this case, because of the higher radiometric resolution of the HSI mosaic, reflectance values for the HSI mosaics capture differences among the vascular plants.

Our band correlation analysis indicates that for most of the bands and dates, there is a variable agreement between HSI and the Sentinel-2A reflectance results (Fig. 11), with correlation coefficient (r) values as high as 0.731 for B8 in May 24th, and as low as 0.129 for the same B8

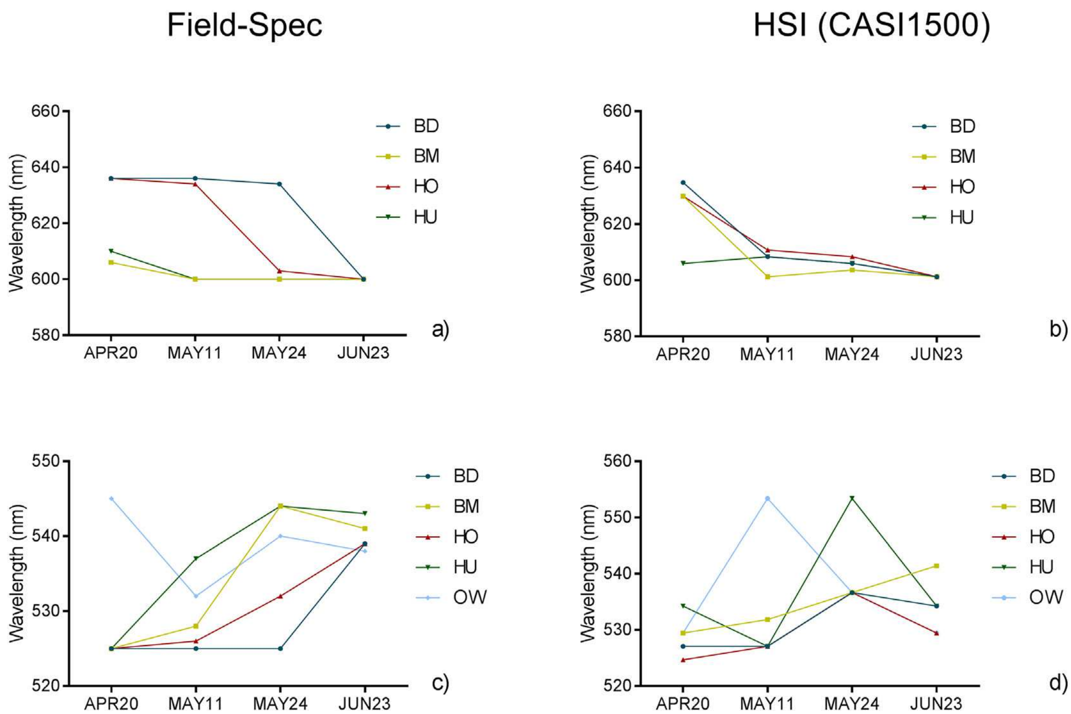

Fig. 8. Phenospectral changes for vegetation physiognomies at two spectral features (600–640 nm and 525–575 nm) for field spectroscopy (a and c, respectively) and the HSI (b and d, respectively) plots. BD: Blue dome, BM: Bog margin, HO: Hollow, HU: Hummock and OW: Open Water. (For interpretation of the references to colour in this figure legend, the reader is referred to the web version of this article.)

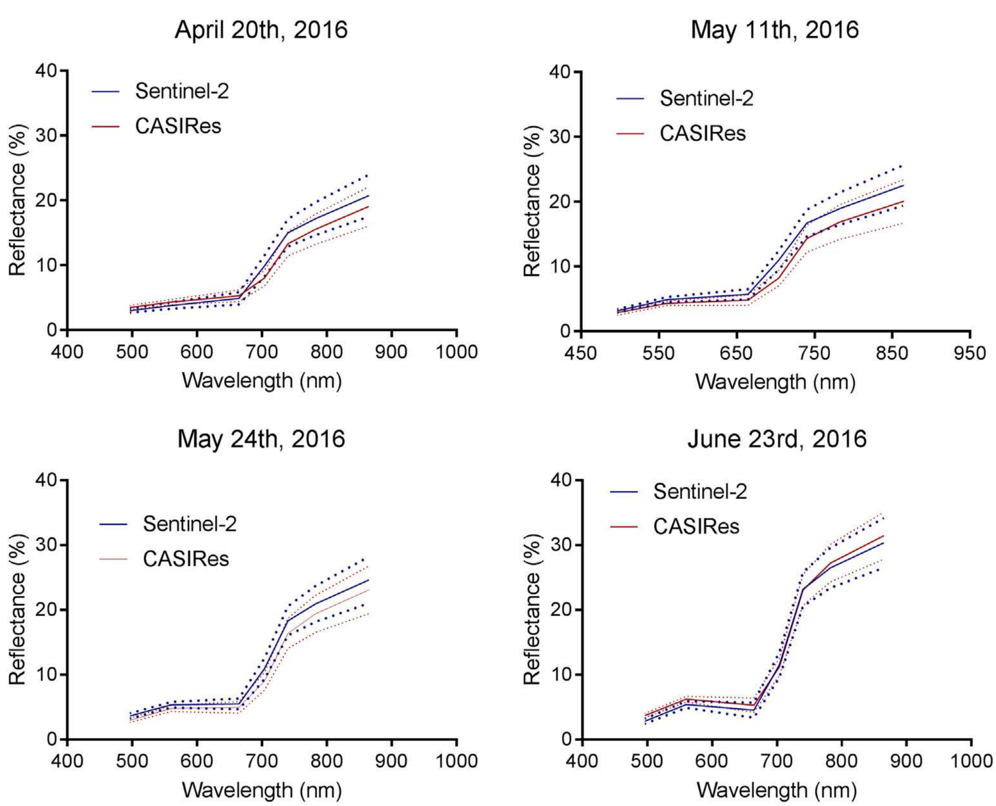

Fig. 9. Comparison between Sentinel-2A and HSI mosaic (CASIRes) (7 spectral bands at 20 m spatial resolution) bottom of the atmosphere reflectance for four dates for the first half of the phenological cycle (i.e. greening) at the Mer Bleue Peatland Observatory in 2016.

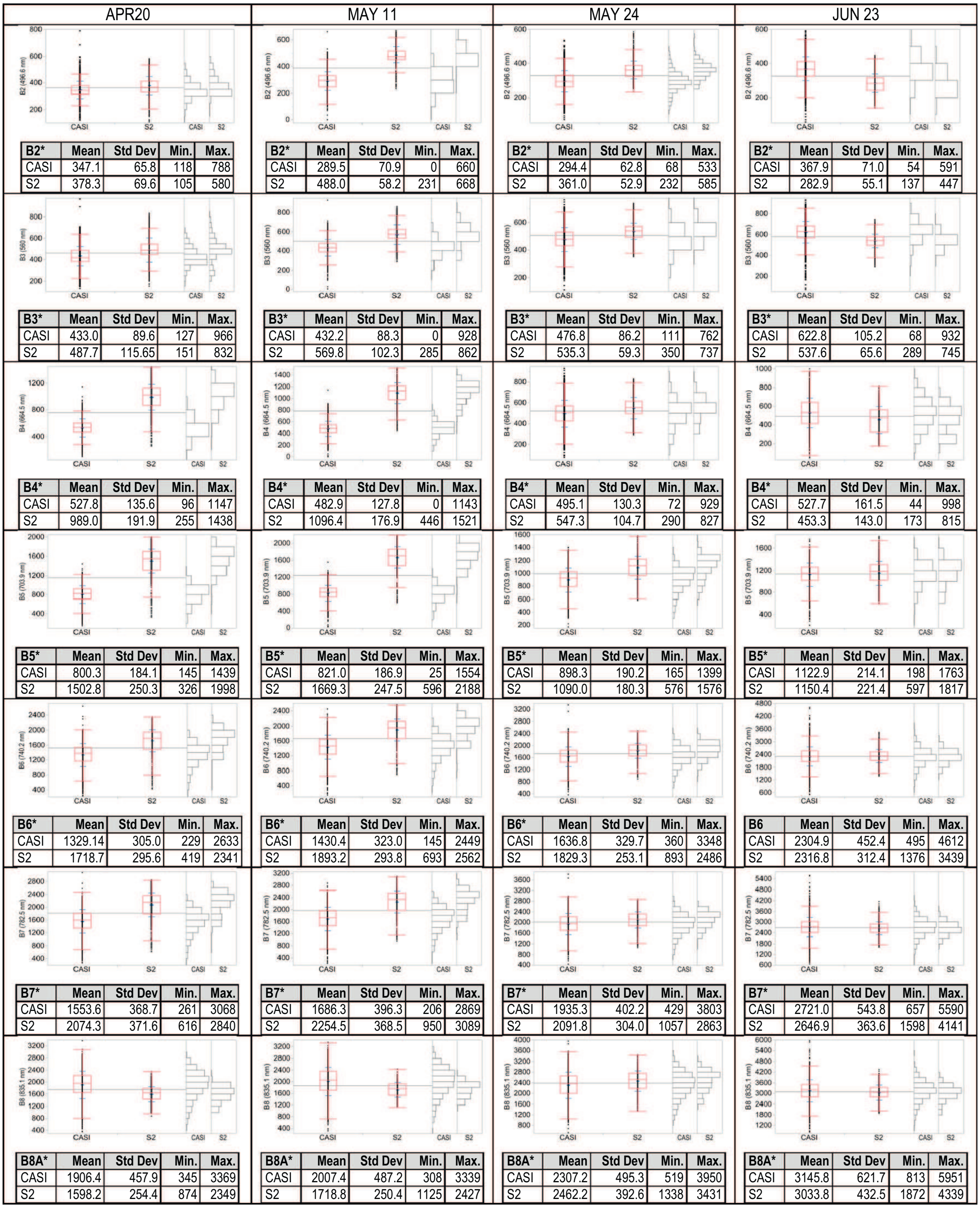

APR20

B2*	Mean	Std Dev	Min.	Max.
CASI	347.1	65.8	118	788
S2	378.3	69.6	105	580

B3*	Mean	Std Dev	Min.	Max.
CASI	433.0	89.6	127	966
S2	487.7	115.65	151	832

B4*	Mean	Std Dev	Min.	Max.
CASI	527.8	135.6	96	1147
S2	989.0	191.9	255	1438

B5*	Mean	Std Dev	Min.	Max.
CASI	800.3	184.1	145	1439
S2	1502.8	250.3	326	1998

B6*	Mean	Std Dev	Min.	Max.
CASI	1329.14	305.0	229	2633
S2	1718.7	295.6	419	2341

B7*	Mean	Std Dev	Min.	Max.
CASI	1553.6	368.7	261	3068
S2	2074.3	371.6	616	2840

B8A*	Mean	Std Dev	Min.	Max.
CASI	1906.4	457.9	345	3369
S2	1598.2	254.4	874	2349

MAY 11

B2*	Mean	Std Dev	Min.	Max.
CASI	289.5	70.9	0	660
S2	488.0	58.2	231	668

B3*	Mean	Std Dev	Min.	Max.
CASI	432.2	88.3	0	928
S2	569.8	102.3	285	862

B4*	Mean	Std Dev	Min.	Max.
CASI	482.9	127.8	0	1143
S2	1096.4	176.9	446	1521

B5*	Mean	Std Dev	Min.	Max.
CASI	821.0	186.9	25	1554
S2	1669.3	247.5	596	2188

B6*	Mean	Std Dev	Min.	Max.
CASI	1430.4	323.0	145	2449
S2	1893.2	293.8	693	2562

B7*	Mean	Std Dev	Min.	Max.
CASI	1686.3	396.3	206	2869
S2	2254.5	368.5	950	3089

B8A*	Mean	Std Dev	Min.	Max.
CASI	2007.4	487.2	308	3339
S2	1718.8	250.4	1125	2427

MAY 24

B2*	Mean	Std Dev	Min.	Max.
CASI	294.4	62.8	68	533
S2	361.0	52.9	232	585

B3*	Mean	Std Dev	Min.	Max.
CASI	476.8	86.2	111	762
S2	535.3	59.3	350	737

B4*	Mean	Std Dev	Min.	Max.
CASI	495.1	130.3	72	929
S2	547.3	104.7	290	827

B5*	Mean	Std Dev	Min.	Max.
CASI	898.3	190.2	165	1399
S2	1090.0	180.3	576	1576

B6*	Mean	Std Dev	Min.	Max.
CASI	1636.8	329.7	360	3348
S2	1829.3	253.1	893	2486

B7*	Mean	Std Dev	Min.	Max.
CASI	1935.3	402.2	429	3803
S2	2091.8	304.0	1057	2863

B8A*	Mean	Std Dev	Min.	Max.
CASI	2307.2	495.3	519	3950
S2	2462.2	392.6	1338	3431

JUN 23

B2*	Mean	Std Dev	Min.	Max.
CASI	367.9	71.0	54	591
S2	282.9	55.1	137	447

B3*	Mean	Std Dev	Min.	Max.
CASI	622.8	105.2	68	932
S2	537.6	65.6	289	745

B4*	Mean	Std Dev	Min.	Max.
CASI	527.7	161.5	44	998
S2	453.3	143.0	173	815

B5*	Mean	Std Dev	Min.	Max.
CASI	1122.9	214.1	198	1763
S2	1150.4	221.4	597	1817

B6	Mean	Std Dev	Min.	Max.
CASI	2304.9	452.4	495	4612
S2	2316.8	312.4	1376	3439

B7*	Mean	Std Dev	Min.	Max.
CASI	2721.0	543.8	657	5590
S2	2646.9	363.6	1598	4141

B8A*	Mean	Std Dev	Min.	Max.
CASI	3145.8	621.7	813	5951
S2	3033.8	432.5	1872	4339

Fig. 10. Sentinel-2A and resampled HSI (CASI-1500) spectral band reflectance comparison across dates. The box plots show the median, and the 25th and 75th percentiles, minimum and maximum values and outliers. The blue lines indicate mean and standard deviation. * indicates *t*-test significant differences ($p < 0.0001$) for all bands and dates with the exception of B6 in June 23rd. Panels on the right hand side show the histogram for the total number of pixels extracted from the twenty 5 × 5 m plots. (For interpretation of the references to colour in this figure legend, the reader is referred to the web version of this article.)

on May 11th. These variations are explained in part by similar factors to those found by Mandanici and Bitelli (2016). First, the spatial heterogeneity generated by the resampling procedure for the HSI could have an effect on the reflectance values, which are a function of vegetation phenological changes and band sensitivity to these changes. In this study, we did not assess the impact of the resampling method directly, but we used the resampled airborne HSI reflectance product to do a preliminary validation of the Sentinel-2A product for assessing phenospectral changes at Mer Bleue. Secondly, we did not co-register the HSI mosaic product to the Sentinel-2A, since a visual assessment showed a good spatial alignment of both datasets, and Mer Bleue has a very flat topography at 20 m resolution. In addition, we assume that our sampling approach (1-ha plots) is sufficient to capture overall vegetation reflectance patterns at the landscape level. Finally, variations in solar azimuth and zenith angles between the HSI mosaics and the Sentinel-2A reflectance products could explain differences between sensors. In a comparative analysis between Sentinel-2A and other moderate resolution sensors, Radoux et al. (2016) found that its spatial and spectral resolutions allowed for accurate separation between foreground-background landscape objects such as grassland, crops, roads,

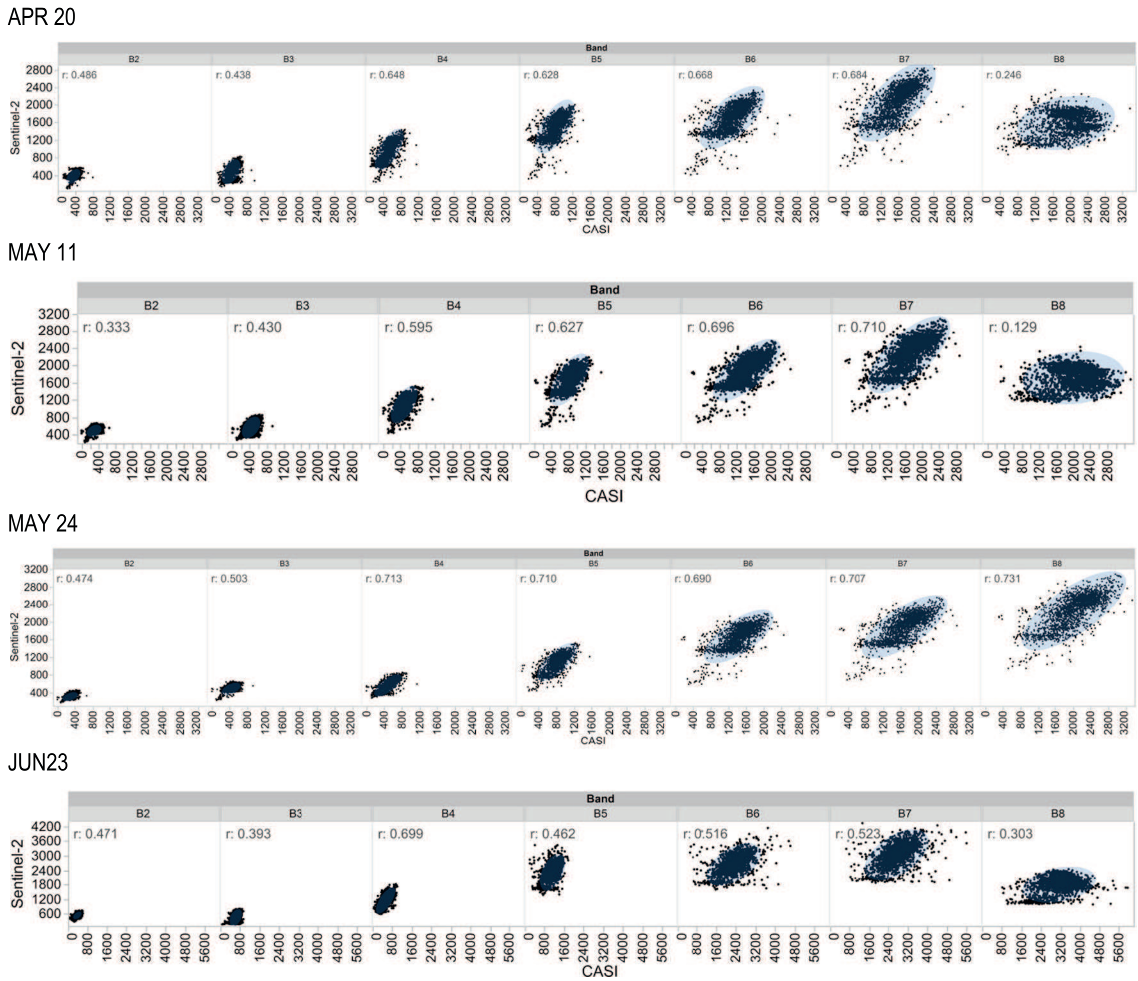

Fig. 11. Sentinel-2A and resampled CASI band correlation analysis for the four dates at MBCA. 95% ellipses are shown for each point cloud as well as the correlation coefficient (r) for each pair-wise evaluation. Values on the axes represent reflectance × 10,000.

Table 7
Single ratio (SR), NDVI and RENDVI statistics for Sentinel-2A and resampled HSI from April to June 2106 at Mer Bleue.

	Sentinel-2				HSI (CASI1500)			
	APR 20	MAY 11	MAY 24	JUN 23	APR 20	MAY 11	MAY 24	JUN 23
SR								
Mean	4.36	3.99	4.57	7.40	3.68	4.29	4.83	6.49
Std. dev	0.65	0.46	0.63	2.77	0.65	1.03	1.08	2.46
Min	2.27	2.38	3.24	4.14	1.52	2.02	2.83	2.78
Max	6.78	5.53	10.15	23.59	7.38	19.96	18.43	28.46
NDVI								
Mean	0.62	0.60	0.64	0.74	0.56	0.61	0.65	0.71
Std. dev	0.05	0.04	0.04	0.06	0.06	0.07	0.05	0.07
Min	0.39	0.41	0.53	0.61	0.21	0.34	0.48	0.47
Max	0.74	0.69	0.82	0.92	0.76	1.00	0.90	0.93
RENDVI								
Mean	0.21	0.21	0.26	0.34	0.25	0.27	0.29	0.34
Std. dev	0.04	0.03	0.03	0.07	0.04	0.05	0.04	0.04
Min	0.10	0.12	0.18	0.22	0.09	0.11	0.18	0.20
Max	0.35	0.32	0.42	0.57	0.40	0.76	0.46	0.48

etc. However, the spatial scale at which the vegetation physiognomies change at Mer Bleue is still finer than what has been shown to be detectable by Sentinel-2A and could be a potential factor in the difference between the resampled HSI mosaics and the Sentinel-2A data both from the multi-band reflectance and vegetation indices.

Vegetation index results illustrate phenospectral trends at Mer Bleue based on the HSI mosaics and Sentinel-2A data, with an increase in the index values from April to June (vegetation greening-up) (Fig. 12). However, higher Sentinel-2A index values are higher for SR and NDVI (Bands 8:835.1 nm and 4:664.5 nm) from April 20th, but not for RE-NDVI (Bands 6:740.2 nm and 5:703.9 nm). At the landscape level, besides the predominant bog areas, Mer Bleue encompasses areas with

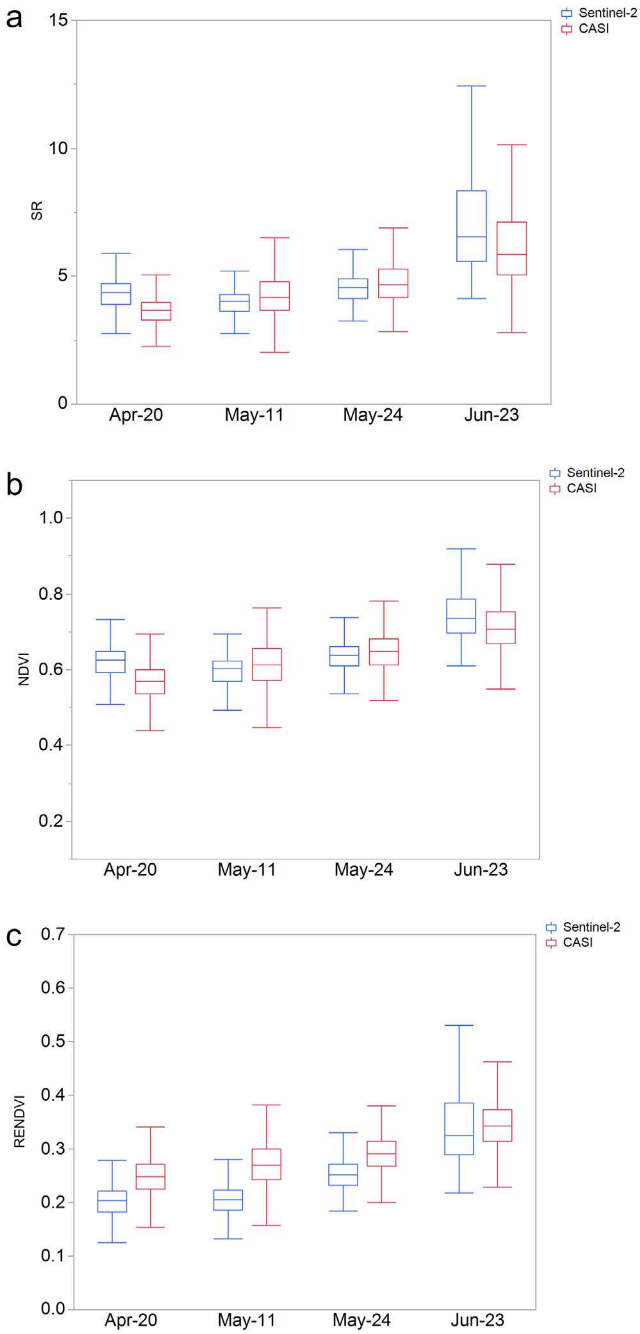

Fig. 12. Comparison of three spectral vegetation indices between Sentinel-2A and the resampled CASI (7 channels at 20 m spatial resolution) the Mer Bleue Research Observatory in 2016: a) SR, b) NDVI and c) RENDVI).

evergreen shrubs as well as areas with mixed forest and forested bog (Sonnentag et al., 2007; Arroyo-Mora et al., 2018), that were captured by our random sampling plots. We theorize that these greener areas drive the higher SR and NDVI values captured at 20 m spatial resolution in Sentinel-2A during April 20th, but not in the HSI mosaics. The higher radiometric and spatial resolution of the HSI, even after resampling to Sentinel-2A sensor characteristics (only spatial and spectral), still captures more subtle mosses and deciduous vascular plants, the brown and red vegetation colour characteristic of early spring, resulting in lower SR and NDVI values. In the case of the RENDVI, it seems to be less sensitive to the aforementioned subtle differences in vegetation for both sensors, and as expected, more sensitive to changes in chlorophyll content (Gitelson and Merzlyak, 1994). Consequently, as the vascular plant green-up and chlorophyll content increases (Kalacska et al., 2015), the RENDVI index value increases. Radoux et al. (2016) found a relative homogeneity of response in spectral vegetation indices with Sentinel-2A, despite their different functions and purposes, a trend we also found with NDVI and SR. One of the strengths of Sentinel-2A over its predecessors, however, is the inclusion of the red-edge bands, which have been shown to improve vegetation class separability (Radoux et al., 2016). Of the three indices tested here, the RENDVI showed the most distinct greening trend as captured by the field spectroscopy data (Fig. 6). Conversely, neither NDVI nor SR captured the expected phenological pattern at the landscape level (Fig. 12).

Future work at Mer Bleue, aiming to capture spectral changes for long term monitoring of phenological patterns and important processes such as the onset of the spring photosynthesis period (Moore et al., 2006), would provide additional information to revisit our preliminary findings. Additional reflectance products such as indices incorporating the SWIR bands of Sentinel-2A should also be examined for their potential to capture landscape scale phenospectral changes in the peatland.

5. Conclusion

In this study, we determined the utility of a multiplatform remotely sensed dataset which included near coincidental data collection from field spectroscopy and airborne hyperspectral imagery, to assess Sentinel-2A reflectance products for measuring short-term phenospectral changes in an ombrotrophic bog. Our bottom-up methodological approach found a good correspondence between in-situ spectral measurements and the atmospherically corrected HSI images for the VIS region for the four dates evaluated here, but not for the NIR region. Although, our in-situ measurements are limited to one area with accessibility for the validation of the HSI data in Mer Bleue, we used full HSI resampled mosaics to compare with Sentinel-2A images for the same dates. At the landscape level (i.e. MBCA), we found that Sentinel-2A reflectance and vegetation indices products capture the short-term phenospectral changes characteristic of Mer Bleue, and are consistent with the HSI resampled products. Further assessment of the Sentinel-2A products should include mid to long term data to evaluate full season phenological patterns and their yearly variations. Given the large extent of northern peatlands and their significant role in storing carbon, Sentinel-2A products could facilitate our understanding of this ecosystem's response to climate change.

Acknowledgments

Funding was provided by the European Space Agency (ESA) Sensor Performance, Products and Algorithms (SPPA) element of the Earth Observation ground segment. We express our appreciation to DRDC-Valcartier for the loan of the CASI instrument and to the National Capital Commission (NCC) for access to Mer Bleue. We thank T.R. Moore for aiding in the definition of the vegetation physiognomies at Mer Bleue, for his feedback on this manuscript and for fruitful discussions about applications of remote sensing in northern peatlands. We also thank Mike Dalva for logistics support at Mer Bleue. We would like to recognize students from the Applied Remote Sensing Laboratory for supporting data collection as well as A. Bergen and D. Inamdar from NRC-FRL. Ms. Kathryn Elmer provided revisions on early stages of this manuscript. This work was also supported by the Natural Sciences and Engineering Research Council of Canada (NSERC) (RGPIN355809-9) and Canada Foundation for Innovation (CFI: 25776 John R. Evans Leaders Fund) (to Kalacska). We thank the reviewers for their comments, which improved the overall quality of the manuscript.

Appendix A

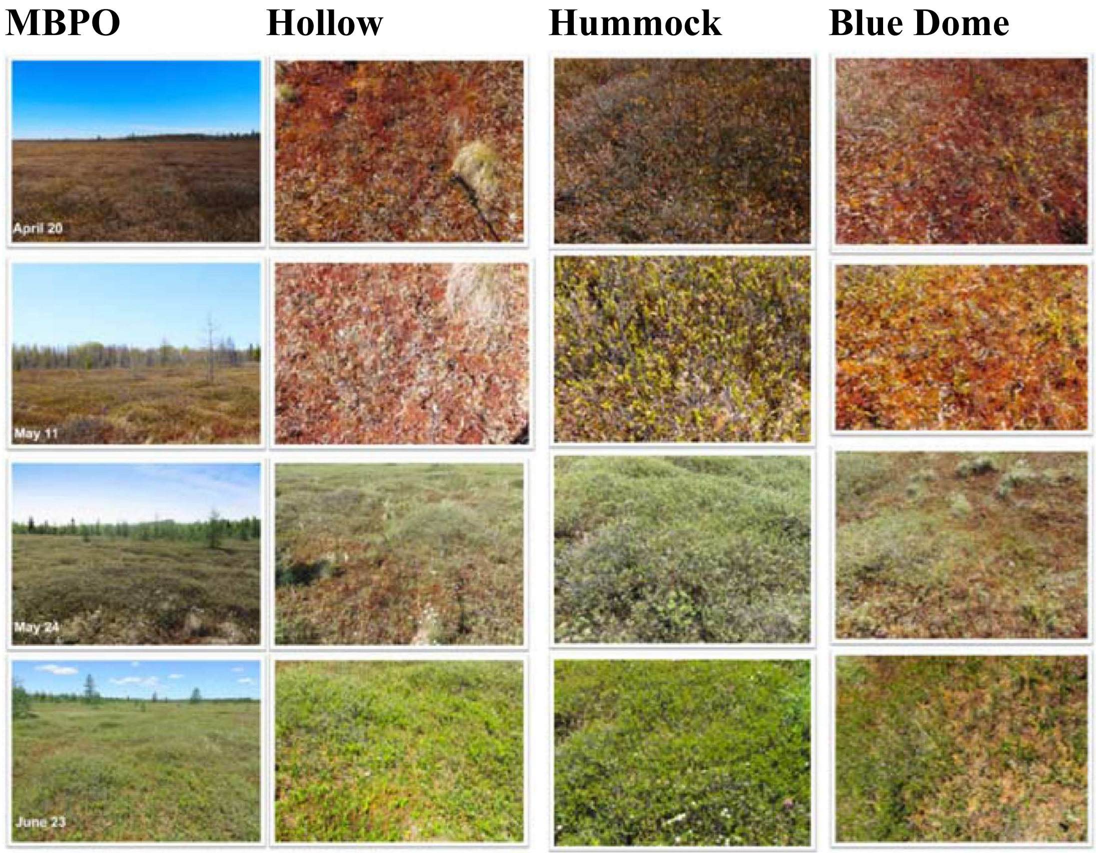

Appendix A1. Phenological changes (i.e. greening up) at the Mer Bleue Peatland Observatory (MBPO) from April 20th to June 23rd, 2016. Site overview photographs and example of a plot photo for hollows (predominately mosses), hummocks (predominately vascular plants) and the Blue dome area (mosses)

References

Arroyo-Mora, J., Kalacska, M., Soffer, R., Moore, T., Roulet, N., Juutinen, S., Ifimov, G., Leblanc, G., Inamdar, D., 2018. Airborne Hyperspectral Evaluation of Maximum Gross Photosynthesis, Gravimetric Water Content, and CO2 Uptake Efficiency of the Mer Bleue Ombrotrophic Peatland. Remote Sens. 10, 565.
Bellisario, L.M., Bubier, J.L., Moore, T.R., Chanton, J.P., 1999. Controls on CH4 emissions from a northern peatland. Glob. Biogeochem. Cycles 13, 81–91.
Belyea, L.R., Malmer, N., 2004. Carbon sequestration in peatland: patterns and mechanisms of response to climate change. Glob. Chang. Biol. 10, 1043–1052.
Birth, G.S., McVey, G.R., 1968. Measuring the color of growing turf with a reflectance spectrophotometer. Agron. J. 60, 640–643.
Brook, A., Dor, E.B., 2011. Supervised vicarious calibration (SVC) of hyperspectral remote-sensing data. Remote Sens. Environ. 115, 1543–1555.
Calmé, S., Desrochers, A., Savard, J.-P.L., 2002. Regional significance of peatlands for avifaunal diversity in southern Québec. Biol. Conserv. 107, 273–281.
Chapman, S., Buttler, A., Francez, A.-J., Laggoun-Défarge, F., Vasander, H., Schloter, M., Combe, J., Grosvernier, P., Harms, H., Epron, D., Gilbert, D., Mitchell, E., 2003. Exploitation of northern peatlands and biodiversity maintenance: a conflict between economy and ecology. Front. Ecol. Environ. 1, 525–532.
Drusch, M., Del Bello, U., Carlier, S., Colin, O., Fernandez, V., Gascon, F., Hoersch, B., Isola, C., Laberinti, P., Martimort, P., Meygret, A., Spoto, F., Sy, O., Marchese, F., Bargellini, P., 2012. Sentinel-2: ESA's optical high-resolution mission for GMES operational services. Remote Sens. Environ. 120, 25–36.
Eppinga, M.B., Rietkerk, M., Borren, W., Lapshina, E.D., Bleuten, W., Wassen, M.J., 2008. Regular surface patterning of peatlands: confronting theory with field data. Ecosystems 11, 520–536.
ESA, 2016. Sentinel online. S2_OPER_MSI_SPECT_20140919T000000_0006.xml. https://earth.esa.int/web/sentinel/user-guides/sentinel-2-msi/document-library/-/asset_publisher/Wk0TKajiISaR/content/sentinel-2a-spectral-responses, Accessed date: 22 November 2016.
Fisher, J.I., Mustard, J.F., Vadeboncoeur, M.A., 2006. Green leaf phenology at Landsat resolution: scaling from the field to the satellite. Remote Sens. Environ. 100, 265–279.
Frolking, S., Talbot, J., Jones, M.C., Treat, C.C., Kauffman, J.B., Tuittila, E.-S., Roulet, N., 2011. Peatlands in the Earth's 21st century climate system. Environ. Rev. 19, 371–396.
Gitelson, A., Merzlyak, M.N., 1994. Quantitative estimation of chlorophyll-a using reflectance spectra: experiments with autumn chestnut and maple leaves. J. Photochem. Photobiol. B Biol. 22, 247–252.
Gorham, E., 1991. Northern peatlands: role in the carbon cycle and probable responses to climatic warming. Ecol. Appl. 1, 182–195.
Harris, A., Bryant, R.G., 2013. Northern peatland vegetation and the carbon cycle: a remote sensing approach. In: Carbon Cycling in Northern Peatlands. American Geophysical Union, pp. 79–98.
Harris, A., Charnock, R., Lucas, R.M., 2015. Hyperspectral remote sensing of peatland floristic gradients. Remote Sens. Environ. 162, 99–111.
ITRES, 2013. Standard Processing & Data QA Manual. pp. 182.
Kalacska, M., Lalonde, M., Moore, T.R., 2015. Estimation of foliar chlorophyll and nitrogen content in an ombrotrophic bog from hyperspectral data: scaling from leaf to image. Remote Sens. Environ. 169, 270–279.
Kalacska, M., Arroyo-Mora, J.P., Soffer, R., Leblanc, G., 2016. Quality control assessment of the mission airborne carbon 13 (MAC-13) hyperspectral imagery from Costa Rica. Can. J. Remote. Sens. 42, 85–105.
Kimes, D.S., Kirchner, J.A., Newcomb, W.W., 1983. Spectral radiance errors in remote sensing ground studies due to nearby objects. Appl. Opt. 22, 8–10.
Kokaly, R.F., Despain, D.G., Clark, R.N., Livo, K.E., 2003. Mapping vegetation in Yellowstone National Park using spectral feature analysis of AVIRIS data. Remote Sens. Environ. 84, 437–456.
Krankina, O.N., Pflugmacher, D., Friedl, M., Cohen, W.B., Nelson, P., Baccini, A., 2008. Meeting the challenge of mapping peatlands with remotely sensed data. Biogeosciences 5, 1809–1820.
Lafleur, P.M., Hember, R.A., Admiral, S.W., Roulet, N.T., 2005. Annual and seasonal variability in evapotranspiration and water table at a shrub-covered bog in southern Ontario, Canada. Hydrol. Process. 19, 3533–3550.
Leifeld, J., Menichetti, L., 2018. The underappreciated potential of peatlands in global climate change mitigation strategies. Nat. Commun. 9, 1071.
Maltby, E., Immirzi, P., 1993. Carbon dynamics in peatlands and other wetland soils regional and global perspectives. Chemosphere 27, 999–1023.
Mandanici, E., Bitelli, G., 2016. Preliminary comparison of Sentinel-2 and Landsat 8 imagery for a combined use. Remote Sens. 8, 1014.
Moore, T.R., Roulet, N.T., Waddington, J.M., 1998. Uncertainty in predicting the effect of climatic change on the carbon cycling of Canadian peatlands. Clim. Chang. 40,

229–245.
Moore, T.R., Lafleur, P.M., Poon, D.M.I., Heumann, B.W., Seaquist, J.W., Roulet, N.T., 2006. Spring photosynthesis in a cool temperate bog. Glob. Chang. Biol. 12, 2323–2335.
Moore, T.R., De Young, A., Bubier, J.L., Humphreys, E.R., Lafleur, P.M., Roulet, N.T., 2011. A multi-year record of methane flux at the Mer Bleue bog, Southern Canada. Ecosystems 14, 646.
Müller-Wilm, U., 2016. Sentinel-2 MSI – Level-2A Prototype Processor Installation and User Manual.
Poulin, M.F., Careau, D., Rochefort, L., Desrochers, A., 2002. From satellite imagery to peatland vegetation diversity: how reliable are habitat maps? Ecol. Soc. 6.
Price, J.C., 1994. How unique are spectral signatures? Remote Sens. Environ. 49, 181–186.
Radoux, J., Chomé, G., Jacques, D., Waldner, F., Bellemans, N., Matton, N., Lamarche, C., D'Andrimont, R., Defourny, P., 2016. Sentinel-2's potential for sub-pixel landscape feature detection. Remote Sens. 8, 488.
Reed, B.C., Schwartz, M.D., Xiao, X., 2009. Remote sensing phenology. In: Noormets, A. (Ed.), Phenology of Ecosystem Processes: Applications in Global Change Research. Springer New York, New York, NY, pp. 231–246.
Richter, R., Schläpfer, D., 2002. Geo-atmospheric processing of airborne imaging spectrometry data. Part 2: atmospheric/topographic correction. Int. J. Remote Sens. 23, 2631–2649.
Roulet, N.T., Lafleur, P.M., Richard, P.J.H., Moore, T.R., Humphreys, E.R., Bubier, J., 2007. Contemporary carbon balance and Late Holocene carbon accumulation in a northern peatland. Glob. Chang. Biol. 13, 397–411.
Rouse, J.W., Haas, R.H., Schell, J.A., Deering, D.W., 1974. Monitoring vegetation systems in the Great Plains with ERTS. In: Proceedings of the Third Earth Resources Technology Satellite-1 Symposium. 317. pp. 301.
Secker, J., Staenz, K., Gauthier, R.P., Budkewitsch, P., 2001. Vicarious calibration of airborne hyperspectral sensors in operational environments. Remote Sens. Environ. 76, 81–92.
Sims, D.A., Gamon, J.A., 2002. Relationships between leaf pigment content and spectral reflectance across a wide range of species, leaf structures and developmental stages. Remote Sens. Environ. 81, 337–354.
Soffer, R., Arroyo-Mora, J.P., Kalacska, M., Ifimov, G., White, H.P., Leblanc, S.G., Nazarenko, D., Leblanc, G., 2017. MBASSS Sentinel-2/Landsat 8 Data Product Validation Project – Final Report. NRC-CNRC. CR-FRL-2016-0130 Revision 1.0.
Sonnentag, O., Chen, J.M., Roberts, D.A., Talbot, J., Halligan, K.Q., Govind, A., 2007. Mapping tree and shrub leaf area indices in an ombrotrophic peatland through multiple endmember spectral unmixing. Remote Sens. Environ. 109, 342–360.
Tarnocai, C., 2006. The effect of climate change on carbon in Canadian peatlands. Glob. Planet. Chang. 53, 222–232.
Teillet, P.M., Fedosejevs, G., Gauthier, R.P., O'Neill, N.T., Thome, K.J., Biggar, S.F., Ripley, H., Meygret, A., 2001. A generalized approach to the vicarious calibration of multiple Earth observation sensors using hyperspectral data. Remote Sens. Environ. 77, 304–327.
Williams, D.C., 1999. Establishment of absolute diffuse reflectance scales using the NPL reference reflectometer. Anal. Chim. Acta 380, 165–172.
Yoon, H.W., Allen, D.W., Eppeldauer, G.P., Tsai, B.K., 2009. The Extension of the NIST BRDF Scale From 1100 nm to 2500 nm. pp. 745204-745204-745212.
Yu, Z.C., 2012. Northern peatland carbon stocks and dynamics: a review. Biogeosciences 9, 4071–4085.